

# Fault-tolerant quantum computing with color codes

Andrew J. Landahl,<sup>1,2,\*</sup> Jonas T. Anderson,<sup>2,†</sup> and Patrick R. Rice<sup>2,3,‡</sup>

<sup>1</sup>*Advanced Device Technologies, Sandia National Laboratories, Albuquerque, NM, 87185, USA*

<sup>2</sup>*Center for Quantum Information and Control, University of New Mexico, Albuquerque, NM, 87131, USA*

<sup>3</sup>*Quantum Institute, Los Alamos National Laboratories, Los Alamos, NM, 87545, USA*

We present and analyze protocols for fault-tolerant quantum computing using color codes. To process these codes, no qubit movement is necessary; nearest-neighbor gates in two spatial dimensions suffices. Our focus is on the color codes defined by the 4.8.8 semiregular lattice, as they provide the best error protection per physical qubit among color codes. We present circuit-level schemes for extracting the error syndrome of these codes fault-tolerantly. We further present an integer-program-based decoding algorithm for identifying the most likely error given the (possibly faulty) syndrome. We simulated our syndrome extraction and decoding algorithms against three physically-motivated noise models using Monte Carlo methods, and used the simulations to estimate the corresponding accuracy thresholds for fault-tolerant quantum error correction. We also used a self-avoiding walk analysis to lower-bound the accuracy threshold for two of these noise models. We present two methods for fault-tolerantly computing with these codes. In the first, many of the operations are transversal and therefore spatially local if two-dimensional arrays of qubits are stacked atop each other. In the second, code deformation techniques are used so that all quantum processing is spatially local in just two dimensions. In both cases, the accuracy threshold for computation is comparable to that for error correction. Our analysis demonstrates that color codes perform slightly better than Kitaev's surface codes when circuit details are ignored. When these details are considered, we estimate that color codes achieve a threshold of 0.082(3)%, which is higher than the threshold of  $1.3 \times 10^{-5}$  achieved by concatenated coding schemes restricted to nearest-neighbor gates in two dimensions [Spedalieri and Roychowdhury, *Quant. Inf. Comp.* **9**, 666 (2009)] but lower than the threshold of 0.75% to 1.1% reported for the Kitaev codes subject to the same restrictions [Raussendorf and Harrington, *Phys. Rev. Lett.* **98**, 190504 (2007); Wang *et al.*, *Phys. Rev. A* **83**, 020302(R) (2011)]. Finally, because the behavior of our decoder's performance for two of the noise models we consider maps onto an order-disorder phase transition in the three-body random-bond Ising model in 2D and the corresponding random-plaquette gauge model in 3D, our results also answer the Nishimori conjecture for these models in the negative: the statistical-mechanical classical spin systems associated to the 4.8.8 color codes are counterintuitively more ordered at positive temperature than at zero temperature.

## I. INTRODUCTION

The promise of fault-tolerant quantum computing is a crowning achievement of quantum information science [1–8]. Under a specific set of noise and control assumptions, the promise is that any ideal quantum circuit of size  $L$  can be simulated to any desired precision  $\varepsilon$  by a faulty quantum circuit whose size is at most  $\mathcal{O}(\varepsilon^{-1}L \log^a L)$  for some (small) constant  $a$ . Fault-tolerant quantum computing protocols are judged by the resources they employ in the course of a simulation. Examples of such resources include the constant  $a$ , the hidden constant in the big- $\mathcal{O}$  notation, and the requirements imposed by the noise and control assumptions. Often protocols are compared by a requirement encapsulated in a single number, the *accuracy threshold*, which is an upper bound on the error probability per elementary operation that a faulty circuit must satisfy for the protocol to work. A variety of fault-tolerant quantum computing protocols have been

developed, with threshold estimates ranging from as low as  $10^{-6}$  [9] to as high as 3% [10–12], depending on the protocol and the noise and control assumptions.

An important control constraint relevant for several quantum computing technologies is that the only multi-qubit gates that are possible are those between nearest-neighbor qubits, where the qubits are laid out in some 2D geometry in which each qubit neighbors a constant number of other qubits. Fault-tolerant quantum computing protocols based on concatenated quantum error-correcting codes have a fractal structure that is not commensurate with such a geometry. Indeed, forcing such codes into a semiregular 2D geometry requires that one introduce a substantial number of additional qubit-movement operations that expose the protocol to more errors, thereby diminishing its accuracy threshold. The largest accuracy threshold of which we are aware for a concatenated-coding protocol in a semiregular 2D geometry is  $1.3 \times 10^{-5}$  [13]; that protocol is based on the concatenated nine-qubit Bacon-Shor code [14] embedded in the 2D square lattice.

Cognizant of the constraints imposed by 2D geometry, Kitaev introduced a family of quantum error-correcting codes called *surface codes* that require only local quantum processing, where locality is defined by

\*alandahl@sandia.gov

†jander10@unm.edu

‡rekniht81@gmail.com

a graph embedded in a surface [15]. Several fault-tolerant quantum computing protocols have been developed around surface codes [16–18], and these protocols have significantly higher accuracy thresholds than their concatenated-coding counterparts. Numerical threshold estimates for surface-code protocols range from 0.75% to 1.1% [17–19]; an analytic proof in Ref. [16] guarantees that it is no less than  $1.7 \times 10^{-4}$ .

Recently Bombin and Martin-Delgado proposed a new family of quantum error-correcting codes they call *color codes* which are also defined to be local relative to a graph embedded in a surface [20]. Specifically, they are defined by face-three-colorable trivalent graphs in the following way: on each vertex of the graph lies a qubit, and for each face  $f$  of the graph, one defines two “stabilizer generators” or “checks,”  $X_f$  and  $Z_f$ .  $X_f$  is the tensor product of Pauli  $X$  operators on each qubit incident on face  $f$ , while  $Z_f$  is the tensor product of Pauli  $Z$  operators on each qubit incident on face  $f$ . The color code’s codespace is defined as the simultaneous  $+1$  eigenspace of each of the check operators.

A fault-tolerant quantum computing protocol based on color codes requires an infinite family of color codes of increasing size in order to be able to simulate arbitrarily large ideal quantum circuits to increasing precision. A natural source for an infinite color-code family is a uniform tiling of the plane by a trivalent face-three-colorable lattice. Such a lattice can be embedded in any orientable surface, although later we will restrict attention to embeddings in planar discs. These “semiregular” or “Archimedean” lattices are described in *vertex notation* as  $r.s.t$ , where each vertex is locally surrounded by an  $r$ -gon, an  $s$ -gon, and a  $t$ -gon. The only possible trivalent face-three-colorable tilings of the plane are the 4.8.8 lattice, the 6.6.6 (hex) lattice, and the 4.6.12 lattice, depicted in Fig. 1 [21].

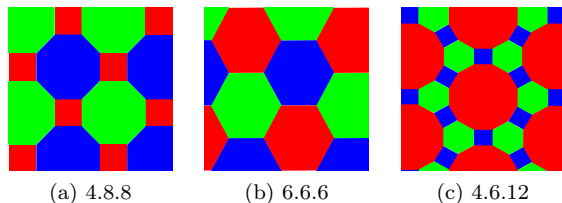


FIG. 1: The three possible face-three-colorable trivalent uniform tilings of the plane.

Accuracy thresholds for fault-tolerant quantum computing have been estimated for color codes in several highly idealized noise models numerically. The values of these thresholds are summarized in Table I, along with analogous estimates for a well-studied surface code and two recently-proposed topological subsystem codes. This table contains numerous gaps, some of which we fill in with the results of this Article—the entries containing our results are highlighted in bold. The most significant gap, which we fill, is an estimate of the accuracy threshold

for noise that afflicts the individual quantum circuit elements used in a fault-tolerant color-code-based quantum computing protocol. The accuracy threshold for noise afflicting the circuit model is perhaps the most instructive of all table entries. This is because this threshold establishes the target error rate per elementary operation that a quantum technology must meet to admit fault-tolerant quantum computation using these codes. It also allows for a fair “apples-to-apples” comparison to the high thresholds estimated for Kitaev’s surface codes in the circuit model.

In this Article, we analyze the accuracy threshold of the 4.8.8 color codes for fault-tolerant quantum computation under several noise and control models. We have restricted our analysis to protocols which use the decoder that identifies the most likely error (MLE) given the error syndrome. We formulate the MLE decoder as an integer program (IP), which in general is NP-hard to solve [33]. Although the decoder is inefficient, it establishes a threshold that we expect is close to the maximum threshold possible for these codes, namely the one obtainable by an optimal decoder, which identifies the most likely logical operation given the error syndrome. For small codes, the MLE IP can be solved “offline” ahead of time to generate a lookup table that can be used during the course of a “live” fault-tolerant quantum computing protocol. Our results comprise both numerical estimates of the accuracy threshold achieved via Monte Carlo simulations and a rigorous lower bound on the accuracy threshold that we prove using combinatorial counting arguments.

The remainder of this Article is organized as follows. In Sec. II, we lay out the control model and the three noise models we consider. In Sec. III, we summarize the properties of the 4.8.8 triangular color codes we study, present two circuit schedules for extracting the error syndrome in these codes, and formulate MLE decoders for these codes as integer programs for each of the noise models that we consider. In Sec. IV, we report our numerical estimates for the accuracy threshold for fault-tolerant quantum error correction of these codes for each of the noise models that we consider. In Sec. V, we use a self-avoiding-walk analysis to prove rigorous lower bounds for the accuracy thresholds of fault-tolerant quantum error correction of these codes against two of the noise models that we consider. In Sec. VI, we relate the quantum error correction accuracy threshold to the quantum computation accuracy threshold for two scenarios: one in which logical qubits are associated with 2D planes that are stacked atop one another like pancakes and the other in which logical qubits are associated with “defects” in a single 2D substrate. In Sec. VII we conclude, summarizing and interpreting our results both in terms of the accuracy thresholds we report and in terms of their consequences for “re-entrant behavior” of an order-disorder phase transition in two associated classical statistical-mechanical models. We cap off our conclusions with some parting thoughts about future directions that we believe are wor-

|                | Code Capacity   |                                   |                                    | Phenomenological                 |               | Circuit-based                         |   |
|----------------|---|-----------------------------------|------------------------------------|----------------------------------|---------------|---------------------------------------|---|
| Code           | Other   | MLE                               | Optimal                            | MLE                              | Optimal       | Other                                 | MLE   |
| 4.8.8          | 8.87 % <sup>a,b</sup> [22]<br>8.7 % <sup>d</sup> [24] | <b>10.56(1) %</b><br>(Our result) | 10.9(2) % [23]<br>10.925(5) % [25] | <b>3.05(4) %</b><br>(Our result) |               | “ $\sim 0.1$ %” <sup>a,b,c</sup> [22] | <b>0.082(3) %</b><br>(Our result)                   |
| 6.6.6          |   |                                   | 10.9(2) % [23]<br>10.97(1) % [25]  |                                  | 4.5(2) % [26] |                                       |   |
| 4.6.12         |   |                                   |                                    |                                  |               |                                       |   |
| 4.4.4.4 Kitaev |   | 10.31(1) % [27]                   | 10.9187 % [28]<br>10.939(6) % [30] | 2.93(2) % [27]                   | 3.3 % [29]    |                                       | 0.75 % <sup>a</sup> [17]<br>1.1 % <sup>a</sup> [19] |
| 3.4.6.4 TSCC   | 1.3 % <sup>a,c</sup> [24]                             |                                   |                                    |                                  |               |                                       |   |
| “SBT” [31]     | 1.3 % <sup>a,c</sup> [31]                             |                                   |                                    |                                  |               |                                       |   |

<sup>a</sup>Reference computes threshold against DP channel, not BP channel. For non-circuit-based noise models, the decoder used does not account for correlations between bit flips and phase flips in DP channel. In these models, we reported the result for the equivalent effective BP channel of strength  $\frac{2}{3}p$ .

<sup>b</sup>Decoder based on hypergraph matching heuristic.

<sup>c</sup>Limited numerics only weakly suggest this value.

<sup>d</sup>Decoder based on mapping to two Kitaev codes.

TABLE I: Numerically-estimated accuracy thresholds for several topological quantum error-correcting codes, noise models, and decoding algorithms. The first three codes (4.8.8, 6.6.6, 4.6.12) are the color codes described in Fig. 1 and its preceding text. The last three codes are the Kitaev surface code on the square lattice [15], a topological subsystem color code on the 3.4.6.4 lattice [32], and a hypergraph-based topological subsystem code proposed by Suchara, Bravyi, and Terhal [31]. The details of the noise models (code capacity, phenomenological, and circuit-based) and decoders (MLE, optimal, and other) are discussed in the text; when possible, results from other references have been translated into one of these models. The notation “ $x.y_1 \cdots y_k(z)\%$ ” means  $x.y_1 \cdots y_k\% \pm (z \times 10^{-k})\%$ . When such notation is not used, it means that the no error analysis was reported in the reference from which the value was drawn.

thy of study.

## II. NOISE AND CONTROL MODEL

The performance of a fault-tolerant quantum computing (FTQC) protocol is strongly influenced by underlying architectural assumptions, so it is important to clearly list what they are. Indeed, when those assumptions are not borne out in real quantum information technologies, an FTQC protocol may fail entirely [34, 35].

Every existing FTQC protocol makes the following architectural assumptions—assumptions which appear to be necessary:

1. **Nonincreasing error rate.** The asymptotic scaling of the error rate as a function of the circuit’s size is nonincreasing. This allows the performance of fault-tolerant circuits to increase asymptotically.
2. **Parallel operation.** The asymptotic parallel-processing rate is larger than a constant times the asymptotic error rate. This allows error correction to keep ahead of the errors.
3. **Reusable memory.** The asymptotic rate at which one can erase or replace qubits is larger than a constant times the asymptotic error rate. This allows entropy to be flushed from the computer faster than it is generated by errors.

Some FTQC protocols also make the following architectural assumptions, which generally lead to higher accuracy thresholds; we make these assumptions here:

4. **Reliable classical computation.** Classical computations always return the correct result.
5. **Fast classical computation.** Classical computations are instantaneous.
6. **No qubit leakage.** Qubits never “leak” out of the computational Hilbert space.
7. **Uncorrelated noise.** Each qubit and gate is afflicted by an independent noise source.

Some additional architectural assumptions, which have a less clear impact on the accuracy threshold, are frequently made as well; we also make these assumptions:

8. **Standard gate basis.** The set of (faulty) quantum gates (including preparation and measurement) available consists of  $|0\rangle$ ,  $|+\rangle$ ,  $I$ ,  $X$ ,  $Z$ ,  $T$ ,  $S$ ,  $CNOT$ ,  $M_Z$ , and  $M_X$ . The definition of what these gates are can be found in standard textbooks, e.g., in Refs. [36, 37].
9. **Equal-time gates.** Each gate, including preparations and measurements, takes the same amount of time to complete.

10. **Uniformly faulty gates.** Each  $k$ -qubit gate, including preparations and measurements, is as equally as faulty as every other  $k$ -qubit gate.

Inspired by the limitations of 2D geometry for some quantum computing technologies, we also make the following assumptions:

11. **2D layout.** Qubits are laid out on a structure describable by a graph embedded in a two-dimensional surface.
12. **Local quantum processing.** Gates can only couple nearest-neighbor qubits in the graph describing their layout.

Finally, we make the following three variants of a thirteenth assumption about the noise model afflicting each gate. Of all the assumptions we make, we have found that this one is most likely to vary in the literature. Commonly-studied alternatives for this assumption include stochastic adversarial noise [38–41], purely depolarizing noise [42], and noise that has a strong bias, such as having phase flips significantly more probable than bit flips [43].

- 13(a). **Circuit-level noise.** Each faulty single-qubit preparation and faulty coherent single-qubit gate ( $|0\rangle$ ,  $|+\rangle$ ,  $I$ ,  $X$ ,  $Z$ ,  $H$ ,  $T$ ,  $S$ ) acts ideally, followed by the bit-flip channel of strength  $p$ , which applies bit flips (Pauli  $X$  operators) with probability  $p$ , followed by the phase-flip channel of strength  $p$ , which applies phase flips (Pauli  $Z$  operators) with probability  $p$ . We call this channel the *BP channel*. Each faulty single-qubit measurement ( $M_X$ ,  $M_Z$ ) acts as the BP channel of probability  $p$  followed by a measurement that returns the incorrect result with probability  $p$ . Importantly, this noise model assumes that the state after a measurement is in an eigenstate of the observable measured, just perhaps not the eigenstate that the measurement indicates. Each *CNOT* gate acts ideally followed by a channel in which each of the 16 two-factor Pauli products ( $II$ ,  $IX$ ,  $XI$ ,  $XY$ , *etc.*) is applied with probability  $p/16$ . We call this channel the *DP channel*. This model differs slightly from a frequently-studied variant in the literature in which each of the 15 nontrivial two-factor Pauli products is applied with probability  $p/15$  and the identity is applied with probability  $1 - p$ .
- 13(b). **Phenomenological noise.** This noise model is the same as the circuit-level noise model (13(a)), except that the circuit for syndrome extraction (described later) is modeled “phenomenologically,” having a probability  $p$  for returning the wrong syndrome bit value. In this model, the propagation of errors between data qubits and between data and ancilla qubits induced by the syndrome extraction circuit are ignored. Single-qubit and two-qubit gates on the data qubits in

circuits other than those used for syndrome extraction (*e.g.*, for encoded computation) are still subject to the BP and DP channels, respectively, as before.

- 13(c). **Code capacity noise.** This model is the same as the phenomenological noise model, except that the syndrome-bit error rate is assumed to be zero. Because there is no need to repeat syndrome measurements in this model, and because the accuracy threshold for “defect-braided” quantum computation is the same as that for quantum memory (as argued later), the accuracy threshold for this noise model is the same as what in quantum information theory is called the single-shot, single-letter quantum capacity for color codes subject to the BP channel.

### III. FAULT-TOLERANT ERROR CORRECTION OF COLOR CODES

#### A. Code family

We confine our analysis of color codes to the 4.8.8 color codes; our choice is motivated by two factors. First, of the three color codes on semiregular 2D lattices, the 4.8.8 code uses the fewest qubits per code distance. Second, the 4.8.8 code is the only one of the three which can realize encoded versions of the entire “Clifford group” [36] of quantum gates, namely the gates which conjugate Pauli operators to Pauli operators in the Heisenberg picture, in a transversal fashion [20], *i.e.*, by applying the same operation to every qubit in a code block or between corresponding qubits in two code blocks. In particular, the gates  $X$ ,  $Z$ ,  $H$ ,  $S$ , and *CNOT* have transversal encoded implementations for these codes. When encoded gates are implemented transversally, fault-tolerant quantum computing protocols for simulating these gates are generally simpler, leading to more favorable accuracy thresholds. The Clifford group of gates is an important group of gates for stabilizer codes such as the color codes, since error correction can be carried out solely using those gates [44].

We further restrict our analysis to *planar* color codes, namely those which are embedded in the disc (a sphere with one puncture). We do this because, for all quantum-computing technologies of which we are aware, arranging qubits on a flat disc is more plausible than arranging them on a more general surface like a torus. The graph constraints defining color codes require that planar color codes have a boundary shaped like a polygon having  $3m$  sides for some positive integer  $m$ . A  $3m$ -sided planar color code encodes  $m$  logical qubits; we restrict attention to the simplest case in which  $m = 1$ . In other words, our focus on this paper is on *triangular* color codes. Examples of three different triangular color codes are depicted in Fig. 2.



The code distance of a triangular color code is equal to its side length, namely the number of qubits along a side of the defining triangle. To see this, notice that the logical  $X$  and  $Z$  operators for the logical qubit are transversal because they are encoded Clifford gates. Thus, when one multiplies a logical  $X$  or  $Z$  operator by all checks of the same Pauli type, except the checks incident on a specified side, one obtains an equivalent logical operator whose Pauli-weight is equal to the that side's length. The family of 4.8.8 triangular codes we study is generated according to the pattern depicted in Fig. 3. Note that the smallest triangular code (for any of three triangular code families depicted in Fig. 2) is equivalent to the well-known Steane  $[[7, 1, 3]]$  code [45]; triangular codes offer a way to generate an infinite code family from the Steane code by a means other than concatenation [72].

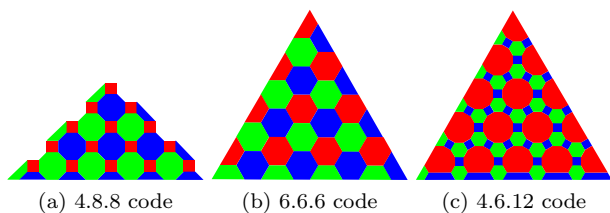


FIG. 2: Three distance  $d = 11$  triangular codes encoding one qubit, drawn from the 4.8.8, 6.6.6, and 4.6.12 lattices respectively. For general  $d$ , these codes have length  $n$  equal to  $\frac{1}{2}d^2 + d - \frac{1}{2}$ ,  $\frac{3}{4}d^2 + \frac{1}{4}$  and  $\frac{3}{2}d^2 - 3d + \frac{5}{2}$  respectively. The asymptotic ratio of  $d^2$  to  $n$  is highest for the 4.8.8 codes.

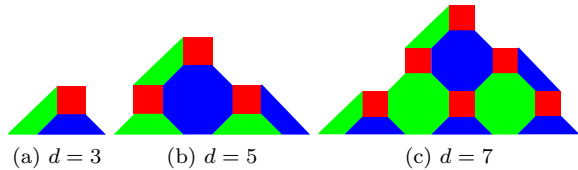


FIG. 3: 4.8.8 color codes of sizes 3, 5, and 7.

Although the colors of the faces in a color code have no intrinsic meaning for the algebraic structure of the code other than constraining the class of graphs on which color codes are defined, it is useful to use the colors as placeholders in discussions from time to time. To that end, we will refer to the colors of the faces as “red,” “green,” and “blue.” We will further assign a color to each edge so that an edge’s color is complementary to the colors of the two faces upon which it is incident. We will call a set of vertices lying on a collection of edges of the same color connected by faces also having that color a “colored chain;” an example of a colored chain is depicted in Fig. 4. We will assign colors to each side of a triangular code so that the color of the side is complementary to the colors of the faces terminating on that side; for example, in Figs. 2 and 3, the left sides of the triangles are blue, the right sides are green, and the bottoms are red. These

side colors are indicated explicitly in Fig. 4.

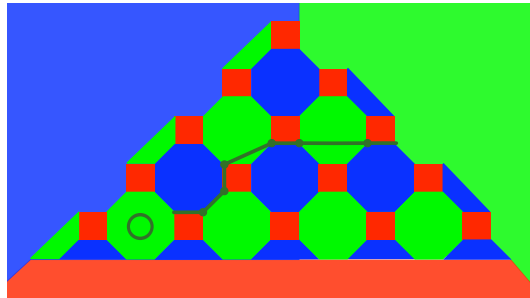


FIG. 4: A green-colored chain in a triangular code. The chain connects a green-colored side of the 4.8.8 triangular code to a green octagonal face. If qubits are flipped (are in error) along this chain, it will only be detected by this terminal octagonal check operator.

## B. Syndrome extraction

To record each error-syndrome bit, the relevant data qubits interact with one or more ancilla qubits and the ancilla qubits are then measured. Shor [1], Steane [46], and Knill [10] have devised elaborate methods for extracting an error syndrome to minimize the impact of ancilla-qubit errors spreading to the data qubits. For topological codes, however, such elaborate schemes are not necessary; a single ancilla qubit per syndrome bit suffices. This is because, by choosing an appropriate order in which data qubits interact with the ancilla qubit, the locality properties of the code will limit propagation of errors to a constant-distance spread. Using more elaborate ancillas is possible, and in general there is a trade-off in the resulting accuracy threshold one must examine between the reduction in error propagation complexity offered versus the additional verification procedures required. Here, we examine the simplest case, with one ancilla qubit per syndrome bit. By placing two syndrome qubits at the center of each face  $f$  (one for the  $X_f$  measurement and one for the  $Z_f$  measurement), the syndrome extraction process can be made spatially local, in keeping with the spirit of the semiregular 2D geometry constraints we are imposing.

Because color codes are Calderbank-Shor-Steane (CSS) codes [47, 48], syndrome bits can be separated into those which identify  $Z$  errors (phase flips) and those which identify  $X$  errors (bit flips). These correspond to the bits coming from measuring the  $X_f$  and  $Z_f$  operators respectively. The circuit for measuring an operator  $X_f$  is identical to the one for measuring the operator  $Z_f$ , except with the basis conjugated by a Hadamard gate; examples of bit-flip and phase-flip extraction circuits for the square faces in the 4.8.8 color code are depicted in Fig. 5.

In a full round of syndrome extraction, both  $X_f$  and  $Z_f$  must be measured for each face  $f$ . One way of schedul-

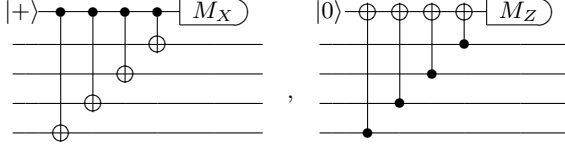


FIG. 5: Six-step circuits for measuring  $X^{\otimes 4}$  and  $Z^{\otimes 4}$ .

ing this is to perform all  $X_f$  measurements in parallel followed by all  $Z_f$  measurements in parallel. The minimal number of steps (ignoring preparation and measurement) for parallel  $X_f$  measurements is eight; an example of such a schedule is depicted in Fig. 6. The  $Z_f$  measurements can be carried out by the same schedule, but in the Hadamard-conjugated basis as depicted in Fig. 5. A complete syndrome extraction round using this schedule then takes 20 steps: 10 for the  $X_f$  measurement and 10 for the  $Z_f$  measurement. For this schedule, one only needs to have one, not two, syndrome qubits at the center of each face.

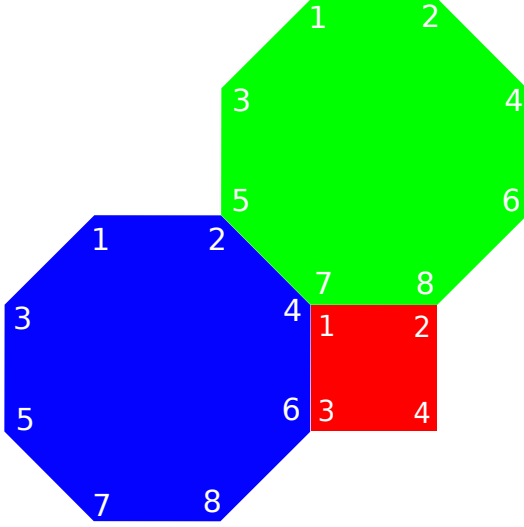


FIG. 6: Simple syndrome extraction circuit schedule. A round of  $X$  checks is followed by a round of  $Z$  checks. The number at each vertex corresponds to the discrete time step in which the physical qubit at that vertex interacts with the syndrome qubit at the face’s center via a  $CNOT$  gate. The same schedule is used for both  $X$  and  $Z$  checks, but with the direction of the  $CNOT$  gates reversed.

The circuit for a full syndrome extraction round can be optimized to use fewer time steps when both syndrome qubits in a face can be processed in parallel. An example of an “interleaved” schedule that uses ten steps is depicted in Fig. 7.

We calculate estimates for the accuracy threshold for both schedules, to assess the impact of compressing the schedule. Some authors who have reported improved thresholds for concatenated-coding schemes using Bacon-Shor codes attribute the improvement in large part to the simplicity of the fault-tolerant Bacon-Shor-

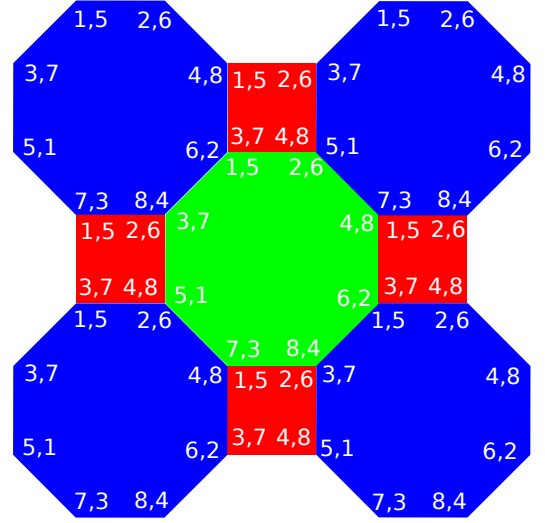


FIG. 7: Schedule with  $X$  and  $Z$  syndromes measured concurrently, in “interleaved” fashion. This schedule takes 8 steps, plus an extra step for syndrome qubit preparations, plus an extra step for syndrome qubit measurements. The label  $m, n$  at a vertex indicates that at time step  $m$  the qubit at that vertex interacts with the  $X$ -syndrome qubit via a  $CNOT$  gate and at time step  $n$  the qubit at that vertex interacts with the  $Z$ -syndrome qubit via a  $CNOT$  gate.

code syndrome-extraction circuit [39]. For color codes, *a priori*, it is not clear that using a simpler syndrome-extraction circuit will yield an analogous improvement. This is because these circuits are not constructed using any fault-tolerant design principles—catastrophic error propagation is halted by the codes’ structure, not by circuit-design principles. It may be the case, in fact, that a simpler circuit will allow errors to propagate to a larger set of qubits than a less simple one. The set of errors to which individual errors are propagated by a syndrome-extraction circuit are called “hooks” in Ref. [16]. An example of how an error can propagate to a “hook” using the schedule of Fig. 7 is depicted in Fig. 8.

Neither the 20-step nor the 10-step schedule is necessarily optimal in the sense of yielding the highest threshold for a fixed number of time steps; we leave that optimization to others. Indeed any schedule that satisfies two constraints is valid: (1) no qubit can be acted upon by two gates at the same time and (2) any stabilizer generator for an error-free input state (including ancilla syndrome qubits) must propagate to an element of the stabilizer group for an error-free output state. Satisfying this second criterion is not trivial; for example, an “obvious” schedule that acts on each face in a clockwise fashion in a manner obeying constraint (1) will not satisfy constraint (2).

The number of steps in the syndrome extraction round can be reduced further to eight steps if we prepare the ancillas for the octagon measurements not in single-qubit states but in cat-states  $(|0\rangle^{\otimes 8} + |1\rangle^{\otimes 8})/\sqrt{2}$  and use Shor’s method of syndrome extraction [1]. (One can also use

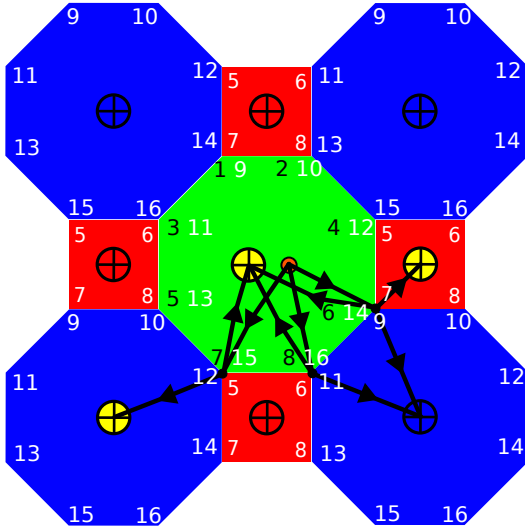


FIG. 8: A single  $X$  error that occurs between time steps five and six on the syndrome qubit for measuring  $X^{\otimes 8}$ , indicated by the small red circle, will propagate to other  $X$  errors according to the arrows. Note that an even number of  $X$  flips is equivalent to no flip at all. Errors that propagate to other syndrome qubits will not propagate further because the syndrome qubits are refreshed before each syndrome extraction round. This particular error causes three data qubits to flip. These flips are correctly detected by the yellow-colored syndrome bits.

four-qubit cat states and create an eight-step schedule, as demonstrated in Ref. [49].) Eight steps is the absolute minimum possible for syndrome extraction, since each qubit must be checked by six different syndrome bits, which must also be prepared and measured. While using cat states reduces the circuit depth, the cat states need to be verified. We opted not to study this schedule because the verification is stochastic, which would lead to a difficult synchronization problem for a large-sized code. That said, such a schedule has the potential to offer a larger accuracy threshold.

Because there is an inherent asymmetry in the order in which we choose to perform  $X_f$  and  $Z_f$  measurements, we will report two threshold results, one for the  $X_f$  measurements and one for the  $Z_f$  measurements. When we only report one value, we are reporting the lower of the two threshold values. For the phenomenological noise model, we choose to model the  $X_f$  and  $Z_f$  syndrome extraction processes as occurring synchronously rather than one followed by the other, since so many of the details of the circuit are washed away in the model anyway. This has the advantage of enabling the accuracy threshold in the phenomenological model to be identified with a phase transition in an associated random-bond Ising model, as described in Ref. [23]. We will discuss this connection in more detail in Secs. IV A and VII B.

Finally, it is worth reminding that the entire syndrome extraction round is repeated a number of times equal to the distance of the code when measurements are allowed

to be faulty, such as in the circuit-level and phenomenological noise models that we study. This ensures that errors in the syndrome bit values can be suppressed as well as errors in the data qubits can be suppressed.

### C. Decoding algorithm

The process of *decoding* refers to a classical algorithm for identifying a recovery operation given an error syndrome, regardless of whether the code from which the syndrome was derived is classical or quantum. Importantly, decoding does not refer to “unencoding,” or performing the inverse of encoding. For classical linear codes, the optimal decoding algorithm is the Most Likely Error (MLE) algorithm, which identifies the recovery operation to be the most likely pattern of bit-flip errors given the syndrome. In general, this algorithm is NP-hard [33], but there are many families of codes for which the algorithm is known to be efficient.

For quantum stabilizer codes, MLE decoding identifies the recovery operation to be the most likely  $n$ -qubit Pauli-group error given the syndrome. (The process of extracting the syndrome forces every error to “collapse” onto a definite  $n$ -qubit Pauli-group operator, which is why it is sufficient to restrict to this family of operators.) MLE decoding is not necessarily optimal for quantum stabilizer codes. This is because quantum error-correcting codes can be *degenerate*, meaning that two distinct correctable errors can map to the same error syndrome. Color codes are examples of highly degenerate codes. The optimal decoding algorithm for quantum stabilizer codes instead identifies the recovery operation to be one that causes the most likely logical operator to be applied after recovery. This is akin to a doctor prescribing medicine that is most likely to cure the ailment rather than prescribing medicine that cures the most likely ailment.

Once a decoding algorithm has identified a recovery operation, which is some  $n$ -qubit Pauli-group operator, it need not necessarily be applied. Because the process of applying the recovery operation is subject to faults, it is wiser to wait until the end of the computation and apply the net recovery operation rather than apply it after each decoding step. One can even propagate the correction past the final qubit measurements at the end of the quantum computation, where the recovery operation becomes completely classical and fault-free. The catch is that one must (classically) adaptively update one’s “Pauli frame” after each decoding iteration by permuting the interpretation of the Pauli operators  $X$ ,  $Y$ , and  $Z$  on each qubit as suggested by the recovery operation. (The Pauli operators get conjugated by the Pauli error identified by the decoder.)

For fault-tolerant quantum error correction and a number of interesting encoded quantum circuits, only Clifford gates are required. Since Clifford gates propagate Pauli operators to Pauli operators in the Heisenberg pic-

ture, one can efficiently track the changing Pauli frame through these gates, as guaranteed by the Gottesman-Knill theorem [50]. One can safely defer applying recovery operations until after final measurement in each of these circuits. However, for universal quantum computation, at least one non-Clifford gate is required. In our protocols, the only such gate we use is the classically-controlled  $S^\dagger$  gate, depicted later in the circuit of Fig. 24. Because this gate propagates a Pauli error to a sum of Pauli errors, it is necessary to actually apply the recovery operation before all but a constant number of these gates in order to prevent the number of terms required to track one's "Heisenberg frame" from growing exponentially.

We develop MLE decoders for triangular 4.8.8 color codes for the three noise model settings we study: code capacity, phenomenological, and circuit-based. For the code-capacity and phenomenological settings, the only operations are single-qubit measurements and identity gates. This means that they involve no circuitry that could map  $X$  errors to  $Z$  errors or vice-versa. Because of this, and because our noise model is one in which single-qubit operations are subject to BP channel noise (which applies  $X$  errors and  $Z$  errors independently), decoding can factor into bit-flip decoding and phase-flip decoding separately. Because color codes are also "strong" CSS codes [37], the MLE decoders for bit-flip and phase-flip errors are in fact identical; for concreteness, we formulate the decoder for  $Z_f$  syndrome bits here.

### 1. Code capacity MLE decoder

In the code-capacity setting, we have a single error-free  $m$ -bit syndrome  $\mathbf{s} = (s_1, \dots, s_m)^T$  where  $s_f = 0$  when  $Z_f$  is measured to have eigenvalue  $+1$  and  $s_f = 1$  when  $Z_f$  is measured to have eigenvalue  $-1$ . (The value of  $m$  is a function of the code size; for the triangular  $n$ -qubit distance- $d$  4.8.8 color code,  $m = (d+1)^2/4 - 1$  and  $n = (d+1)^2/2 - 1$ .) We assign a binary variable  $x_v$  to each vertex  $v$  indicating whether or not the recovery operation calls for the qubit at vertex  $v$  to be bit-flipped (have Pauli  $X$  applied). The objective of MLE decoding is to minimize the number of  $x_v$  variables that are assigned the value 1 subject to the constraint that the parity of the  $x_v$  variables on each face is consistent with the observed syndrome. This can be expressed as the following mathematical optimization problem:

$$\min \sum_v x_v \quad (1)$$

$$\text{sto } \bigoplus_{v \in f} x_v = s_f \quad \forall f \quad (2)$$

$$x_v \in \mathbb{B} := \{0, 1\}. \quad (3)$$

This optimization problem can be expressed as a linear binary integer program (IP) over the finite field  $GF(2)$

as follows:

$$\min \mathbf{1}^T \mathbf{x} \quad (4)$$

$$\text{sto } H\mathbf{x} = \mathbf{s} \bmod 2 \quad (5)$$

$$\mathbf{x} \in \mathbb{B}^n, \quad (6)$$

where  $\mathbf{1}$  denotes the all-ones vector and  $H$  is the parity check matrix associated with the  $Z_f$ -checks. (For color codes, this is the face-vertex incidence matrix.)

To take advantage of well-developed numerical optimization software, it is helpful to replace the linear algebra over  $GF(2)$  in this mathematical program with linear algebra over  $\mathbb{R}$ . One way to do this is to introduce "slack variables" into the optimization problem. Because each check operator in the code has Pauli weight four or Pauli weight eight, each row of  $H$  has Hamming weight four or Hamming weight eight. This means that the  $f$ th component of the vector on the left hand side of constraint (5) is a sum of four or eight binary  $x_v$  variables that must equal  $s_f$  modulo 2. The modulo 2 restriction can be dropped by replacing  $\mathbf{s}$  by  $\mathbf{s} + 2\mathbf{z}_1 + 4\mathbf{z}_2 + 8\mathbf{z}_3$  in the constraint, where the  $\mathbf{z}_i$  are binary "slack variable" vectors that allow the LHS to sum to any integer from  $0 \dots 15$ . While there can be many degenerate solutions to this revised optimization problem having different  $\mathbf{z}_i$  values, any solution generates the same optimal  $\mathbf{x}$  as before. By combining the  $\mathbf{z}_i$  variables and the  $\mathbf{x}$  variables into a single vector  $\mathbf{y} = (\mathbf{x}^T, \mathbf{z}_1^T, \mathbf{z}_2^T, \mathbf{z}_3^T)^T$ , the slack-variable version of the program becomes the following linear binary integer program in which the variables are restricted to be binary but in which the linear algebra is over  $\mathbb{R}$ :

$$\min \mathbf{c}^T \mathbf{y} \quad (7)$$

$$\text{sto } A\mathbf{y} = \mathbf{s} \quad (8)$$

$$\mathbf{y} \in \mathbb{B}^n, \quad (9)$$

where  $\mathbf{c}$  is a vector containing  $n$  ones followed by  $3m$  zeros and  $A$  is the matrix generated by adjoining matrices to  $H$  as

$$A := \left( H \mid -2I \mid -4I \mid -8I \right), \quad (10)$$

in which each  $I$  denotes the  $m \times m$  identity matrix.

There are a number of symmetries that color codes possess which allow one to significantly reduce the complexity of this binary IP. For example, if  $\mathbf{y}$  satisfies the constraints of the IP, then so does  $\mathbf{y}$  with any number of faces complemented. Since complementing the face of any optimal solution will not reduce its weight, we know that each face's sum will never be more than half the weight of that face. This means that for any particular instance of the IP specified by the syndrome vector  $\mathbf{s}$ , the sums for the octagon and square faces can only take the syndrome-dependent values listed in Table II, thereby reducing the number of slack variables required. We take advantage of these kind of symmetries in the software we developed code for estimating the code capacity of 4.8.8 triangular color codes. For example, we never need to



|         | Octagon | Square |
|---------|---------|--------|
| $s = 0$ | 0, 2, 4 | 0, 2   |
| $s = 1$ | 1, 3    | 1      |

TABLE II: Possible values octagonal and square face check sums can take for an optimal IP solution if the face check sum's parity  $s$  is fixed.

use three slack variables and some times we need none at all.

Maximum likelihood decoding is generally an NP-hard problem, and the color codes do not appear to fall into an “easy” subset of instances. This is unfortunate because their close cousins, the surface codes, do have efficient MLE decoders that can be solved as a minimum-weight perfect matching problem [16]. Nevertheless, we can solve the associated IP for reasonably small instance sizes.

## 2. Phenomenological noise MLE decoder

In the phenomenological noise model, the syndrome values themselves can be faulty so we repeat the syndrome extraction process a number of times equal to the distance of the code. In this setting, it is the *difference* in syndrome bit values from one time step to the next rather than the absolute values at particular times step that indicate data errors. This is because a single data error at one time step will lead to flipped syndrome bits for all future time steps (assuming that the syndrome extraction is not faulty), and such a syndrome-bit history should not imply that data errors occurred at each time step—it should imply that a data error occurred only at the time step when the syndrome bit first changed its value. The difference in persistence between data and syndrome errors is depicted in Fig. 9. The input to a MLE decoder is therefore the collection of syndrome *difference* vectors for all time steps, namely

$$\Delta \mathbf{s}_t = \mathbf{s}_t - \mathbf{s}_{t-1} = (\mathbf{s}_t + \mathbf{s}_{t-1}) \bmod 2 \quad \forall t, \quad (11)$$

where  $\mathbf{s}_0 := \mathbf{0}$ .

For a distance  $d$  color code, the optimization problem to solve is again to minimize the number of errors given the observed syndrome, except we now have  $d$  time steps' worth of data-error vectors,  $\mathbf{x}_1, \dots, \mathbf{x}_d$ , and  $d$  time steps' worth of syndrome-error vectors,  $\mathbf{r}_1, \dots, \mathbf{r}_d$ , as variables in the optimization problem. Mathematically, we can write the optimization problem as

$$\min \sum_t \mathbf{1}^T \mathbf{x}_t \quad (12)$$

$$\text{sto } (H\mathbf{x}_t + \mathbf{r}_t + \mathbf{r}_{t-1}) \bmod 2 = \Delta \mathbf{s}_t \bmod 2 \quad \forall t \quad (13)$$

$$\mathbf{x} \in \mathbb{B}^n. \quad (14)$$

As we did for the code-capacity scenario, we can collect these constraints into a single constraint and add slack

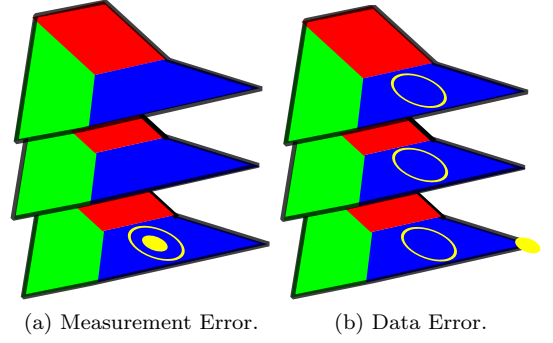


FIG. 9: If syndrome qubits are also allowed to be in error, we repeat syndrome measurements. Time advances from bottom to top. Yellow circles indicate syndrome bits with the value 1. Solid yellow circles indicate bit-flip errors.

variables to make the problem a linear binary IP over the reals. Because the left-hand side of the constraints in Eq. (13) can sum to up to ten for octagon constraints and up to six for square constraints, three slack variables again suffice, allowing us to formulate the optimization problem as

$$\min \mathbf{c}^T \mathbf{y} \quad (15)$$

$$\text{sto } A\mathbf{y} = \Delta \mathbf{s} \quad (16)$$

$$\mathbf{y} \in \mathbb{B}^n, \quad (17)$$

where  $\mathbf{c}$  is a vector containing  $(n+m)d$  ones followed by  $3md$  zeros,  $\Delta \mathbf{s}$  is the vector  $(\Delta \mathbf{s}_1^T, \dots, \Delta \mathbf{s}_d^T)^T$ ,  $\mathbf{y}$  is the vector  $(\mathbf{x}_1^T, \dots, \mathbf{x}_d^T, \mathbf{r}_1^T, \dots, \mathbf{r}_d^T, \mathbf{z}_1^T, \mathbf{z}_2^T, \mathbf{z}_3^T)^T$  and  $A$  is the matrix

$$A = \left( \begin{array}{ccc|ccc|ccc|ccc} H & & & I & & & & & & & \\ & H & & I & I & & & & & & \\ & & \ddots & & & \ddots & & & & & \\ & & & H & & & I & I & & & \end{array} \middle| \begin{array}{c} -2I \\ -4I \\ -8I \end{array} \right). \quad (18)$$

Finally, as we did for the code capacity setting, we can use symmetries to reduce the complexity of solving this IP; Table III summarizes what the possible values are for the square-faced and octagonal-faced constraints.

|         | Octagon    | Square  |
|---------|------------|---------|
| $s = 0$ | 0, 2, 4, 6 | 0, 2, 4 |
| $s = 1$ | 1, 3, 5    | 1, 3    |

TABLE III: Possible values octagonal and square face check sums can take for an optimal IP solution if the face check sum's parity  $s$  is fixed.

### 3. Circuit-level decoder

In the circuit-level noise model, each component of the syndrome extraction circuit can fail with a probability that is a function of a parameter  $p$ , so that the overall probability of a syndrome bit being in error,  $p_s$ , is a complicated function of  $p$ . Even more dauntingly, the circuits can induce correlated errors between syndrome bits and between syndrome bits and data qubits. The phenomenological-noise model does not capture these noise correlations.

We developed an MLE decoder for the circuit-level noise model that accounts for both these induced error correlations and the fact that in this noise model, single-qubit operations are subject to BP-channel noise while *CNOT* gates are subject to DP-channel noise. However, this decoder uses exponentially many more constraints than the phenomenological decoder as a function of code size. Because the IP decoder is already NP-hard, we opted not to study this truly MLE decoder but rather use the phenomenological-noise MLE decoder, which ignores these subtleties. Taking correlations into account will likely boost the accuracy threshold, but probably not by large factors [51]. By way of comparison, the threshold for the square-lattice surface code in the circuit-level noise model is 0.68% when the phenomenological decoder is used [52] (0.75% [17] when using a non-MLE decoder that takes into account some entropic effects), a threshold value that has recently been boosted to 1.1% [19] by accounting for some of the correlations in the noise. We leave the refinement of true MLE decoding of this noise model to others.

## IV. NUMERICAL ESTIMATE OF THE ACCURACY THRESHOLD FOR FAULT-TOLERANT QUANTUM ERROR CORRECTION

### A. Code capacity noise model

Because the  $[[n, 1, d]]$  triangular 4.8.8 color codes are CSS codes, when they are subject to BP-channel noise of strength  $p$ , their code capacity is the same as their bit-flip or phase-flip capacity; we focus on the bit-flip capacity here for definiteness. The number of distinct bit-flip syndromes is  $2^{(n-1)/2}$  and the number of distinct bit-flip errors is  $2^n$ . For small  $n$ , one can pre-solve the MLE decoding IP for each of the  $2^{(n-1)/2}$  distinct bit-flip syndromes. One can then iterate through each of the  $2^n$  distinct error patterns, compute its syndrome, and determine whether the combination of the error pattern plus the inferred correction by the IP leads to a logical

operator, indicating failure of the decoding algorithm. Since error-correction is assumed to be error-free in this noise model, the corrected state is guaranteed to be in the codespace. Because (a) the logical bit-flip operator is transversal, (b) all stabilizer group elements have even weight, and (c) there are an odd number of qubits in every triangular code, it follows that one can identify a decoding failure quickly by computing whether the parity of the error pattern equals the parity of its IP-inferred correction; this means that it suffices to just store the parity of the inferred correction for each pre-computed IP instance. The probability of failure,  $p_{\text{fail}}$  is therefore

$$p_{\text{fail}} = \sum_{\text{failing patterns } E} p^{|E|} (1-p)^{n-|E|}, \quad (19)$$

where  $|E|$  denotes the Hamming weight of the bit-flip error pattern  $E$ .

We carried out this tabulation for the smallest triangular 4.8.8 color codes of distances 1, 3, 5, and 7 (corresponding to 1, 7, 17, and 31 qubits respectively) and computed the corresponding exact polynomials. To speed up the computation, we used several symmetries. For example, it suffices to examine only half of the error patterns because if the decoding algorithm succeeds on an error pattern, it fails on its complement and vice versa. Also, up to overall complementation, every error pattern can be uniquely expressed as the modulo-2 sum of an IP-inferred minimal-weight error pattern and a pattern where a bit-flip stabilizer group element has support. Finally, the decoding algorithm is guaranteed to work on all errors whose weight is less than the code's distance, so those error patterns do not need to be examined.

The formulas we obtained for the smallest codes of distance 1, 3, and 5 (code sizes 1, 7, and 17) are:

$$p_{\text{fail}}^{(1)} = p \quad (20)$$

$$p_{\text{fail}}^{(3)} = p^7 + 7p^6(1-p) + 28p^4(1-p)^3 \quad (21)$$

$$+ 7p^3(1-p)^4 + 21p^2(1-p)^5 \quad (22)$$

$$p_{\text{fail}}^{(5)} = p^{17} + 17p^{16}(1-p) + 136p^{15}(1-p)^2 \quad (23)$$

$$+ 348p^{14}(1-p)^3 + 725p^{13}(1-p)^4 \quad (24)$$

$$+ 3861p^{12}(1-p)^5 + 4764p^{11}(1-p)^6 \quad (25)$$

$$+ 12136p^{10}(1-p)^7 + 9747p^9(1-p)^8 \quad (26)$$

$$+ 14563p^8(1-p)^9 + 7312p^7(1-p)^{10} \quad (27)$$

$$+ 7612p^6(1-p)^{11} + 2327p^5(1-p)^{12} \quad (28)$$

$$+ 1655p^4(1-p)^{13} + 332p^3(1-p)^{14}. \quad (29)$$

The formula we obtained for the distance-7 triangular 4.8.8 color code (31 qubits) is a bit more hefty:

$$\begin{aligned}
p_{\text{fail}}^{(7)} = & p^{31} + 31p^{30}(1-p) + 465p^{29}(1-p)^2 + 4495p^{28}(1-p)^3 + 25658p^{27}(1-p)^4 + 96790p^{26}(1-p)^5 \\
& + 344858p^{25}(1-p)^6 + 1288630p^{24}(1-p)^7 + 3742943p^{23}(1-p)^8 + 10488241p^{22}(1-p)^9 \\
& + 21436239p^{21}(1-p)^{10} + 44259329p^{20}(1-p)^{11} + 67781868p^{19}(1-p)^{12} + 106951476p^{18}(1-p)^{13} \\
& + 127137964p^{17}(1-p)^{14} + 155845748p^{16}(1-p)^{15} + 144694447p^{15}(1-p)^{16} + 138044561p^{14}(1-p)^{17} \\
& + 99301599p^{13}(1-p)^{18} + 73338657p^{12}(1-p)^{19} + 40412986p^{11}(1-p)^{20} + 22915926p^{10}(1-p)^{21} \\
& + 9671834p^9(1-p)^{22} + 4145782p^8(1-p)^{23} + 1340945p^7(1-p)^{24} + 391423p^6(1-p)^{25} + 73121p^5(1-p)^{26} \\
& + 5807p^4(1-p)^{27}.
\end{aligned} \tag{30}$$

Our computing resources did not allow us to compute the exact polynomial for the next-sized code (distance 9 code on 49 qubits), so we resorted to a Monte Carlo estimate for  $p_{\text{fail}}(p)$ . We did this by first selecting three values of  $p$  near where we believed the threshold to be. For each  $p$ , we generated  $N$  trial error patterns drawn from the Bernoulli distribution, namely in which we applied a bit-flip on each of the  $n$  qubits with probability  $p$ . We then inferred the syndrome for each error pattern and checked whether or not it led to a decoding failure for the MLE decoder. The optimal unbiased estimator for  $p_{\text{fail}}$  that we used is

$$p_{\text{fail}}^{(\text{est})} = \frac{N_{\text{fail}}}{N} \tag{31}$$

with a variance of

$$(\sigma_{\text{fail}}^2)^{(\text{est})} = \frac{p_{\text{fail}}^{(\text{est})} (1 - p_{\text{fail}}^{(\text{est})})}{N}. \tag{32}$$

To get reasonably small error bars in these estimates, given where we believed the threshold to be, we chose  $N = 10^5$ . The polynomials for  $p_{\text{fail}}(p)$  are plotted in Fig. 10, including our three points of Monte Carlo data. From these plots, we estimate the accuracy threshold for this noise model to be 10.56(1)%. The error we report in this value comes from the error analysis method we describe in detail in the next section.

To put our result in context, we reference Table I. The threshold value of 10.56(1)% we find is slightly higher than the corresponding MLE threshold for the code capacity 10.31(1)% of 4.4.4.4 surface codes. Intuitively this makes sense, as the 4.8.8 color code has both weight-8 and weight-4 stabilizer generators, both of which are modeled as being measured instantaneously and ideally. Being able to measure high-weight generators quickly should improve the performance of a code, which is the effect we observe.

Our threshold is also less than the threshold value of 10.925(5)% for optimal decoding, which is also not surprising. As with the 4.4.4.4 surface codes, the reduction in threshold is not very significant. For both the surface codes and the 4.8.8 color codes, the accuracy threshold in the code capacity noise model corresponds to a

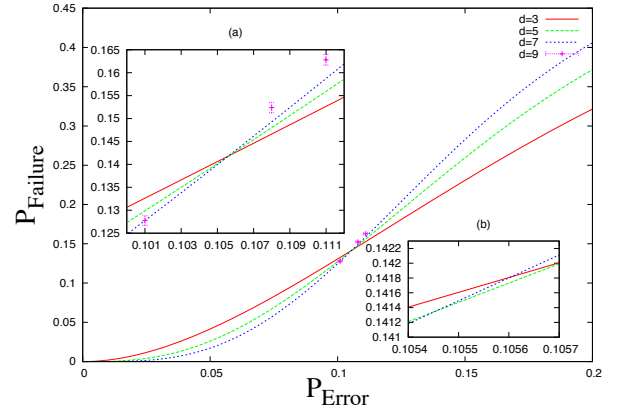


FIG. 10: Code capacity for the 4.8.8 triangular color codes.  $p_{th} = 10.56(1)\%$ . Error bars on Monte Carlo data reflect  $10^5$  instances studied at each of the three corresponding values of  $p$ . The inset figures are zoom-ins near the crossing point to show greater resolution there.

phase transition in a random-bond Ising model (RBIM) of classical spins [16, 23]. For the color codes, the Ising model features 3-body interactions, whereas for the surface codes, the Ising model features 2-body interactions. The MLE decoder in both settings corresponds to the order-disorder transition in the spin model at zero temperature, whereas the optimal decoder corresponds to the order-disorder transition at the temperature along the so-called “Nishimori line,” where the randomness in the bond couplings equals the randomness in the state arising from finite temperature fluctuations. In both the surface-code and color-code settings, the small decrease in accuracy threshold when going from optimal to MLE decoding reflects that the phase-boundary in these models is re-entrant, but only by a small amount. Our results therefore imply a violation of the so-called Nishimori conjecture [53, 54], which conjectures that the spin model shouldn’t become more ordered as the temperature increases. The violation that our results imply is depicted in cartoon fashion in Fig. 11. To our knowledge, the vio-

lation of the Nishimori conjecture for the 3-body RBIM is unknown before our work. We expand more on this connection in Sec. VII B.

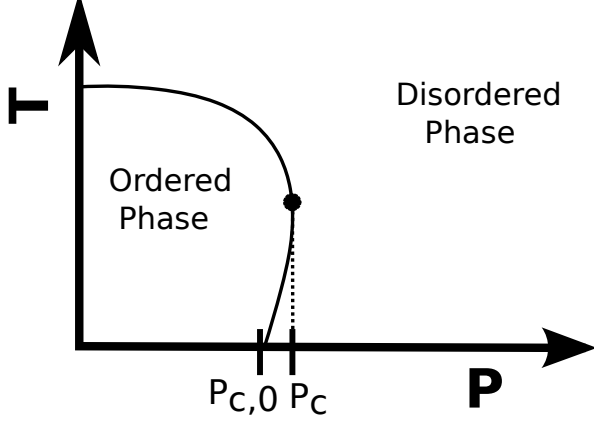


FIG. 11: Phase diagram for 3-body random-bond Ising model. The dark circle is called the Nishimori point. The dotted line is the expected phase boundary given by the Nishimori conjecture. Our value of code capacity (10.56(1)%) establishes that the  $T = 0$  intercept is  $P_{c,0}$ , while results of Ohzeki [25] (10.925(5)%) establish that the Nishimori point occurs at  $P_c$ . Because  $P_c \neq P_{c,0}$ , the Nishimori conjecture for this model is false.

### B. Phenomenological noise model

In the phenomenological noise model, our fault-tolerant quantum error correction protocol repeats syndrome extraction multiple times to increase the reliability of the syndrome bits. This causes the number of possible error patterns for a given code size to grow so rapidly that obtaining exact curves for  $p_{\text{fail}}(p)$  even for small code sizes is intractable. We therefore resorted to Monte Carlo estimates for these curves for even the smallest code sizes. The specific Monte Carlo algorithm we used for computing  $p_{\text{fail}}$  at a fixed value of  $p$  is listed in Algorithm 1.

In words, Algorithm 1 creates an estimator for  $p_{\text{fail}}$  by assessing the performance of many simulated trials of faulty quantum error correction. In each trial, errors are laid down, giving rise to an observed syndrome history. From the syndrome history, a correction is inferred. The actual error history and the inferred error history are XORed onto a single effective time slice, but the state in this effective time slice is not necessarily in the codespace. To achieve this, a fictional ideal (error-free) round of error correction is simulated. If this succeeds (*i.e.*, if it does not generate a logical bit-flip operation), then the trial is deemed a success; otherwise it is deemed a failure. By repeating many trials, one obtains an optimal unbiased estimator for the failure probability  $p_{\text{fail}}$ , with mean and variance given by Eqs. (31–32), identical to the formulas relevant in the code capacity noise model setting.

Our plots of  $p_{\text{fail}}$  versus  $p$  for small-distance color codes

---

#### Algorithm 1 : $p_{\text{fail}}(p)$ by Monte Carlo

---

```

1:  $n_{\text{faces}} \leftarrow \frac{1}{4}(d+1)^2 - 1$ .
2: for  $i = 1$  to  $N$  do
3:   // Generate data and syndrome errors for  $d$  time slices.
4:   for  $t = 1$  to  $d$  do
5:     for  $j = 1$  to  $n$  do
6:        $E[t, j] \leftarrow 1$  with probability  $p$ . // Data errors.
7:     end for
8:     for  $j = n + 1$  to  $n + 1 + n_{\text{faces}}$  do
9:        $E[t, j] \leftarrow 1$  with probability  $p$ . // Synd. errors.
10:    end for
11:  end for
12:   $E_{\text{min}} \leftarrow \text{Decode}(\text{Syndrome}(E))$ . // 3D error volume.
13:   $E' \leftarrow \bigoplus_t E[t] \oplus E_{\text{min}}[t]$ . // 2D error plane.
14:   $E'_{\text{min}} \leftarrow \text{Decode}(\text{Syndrome}(E'))$ . // Ideal decoding.
15:  if  $(\bigoplus_i E'[i] \oplus E'_{\text{min}}[i] = 1)$  then
16:     $N_{\text{fail}} \leftarrow N_{\text{fail}} + 1$ .
17:  end if
18: end for
19: return  $p_{\text{fail}}^{(\text{est})} = N_{\text{fail}}/N$ .
```

---

are depicted in Fig. 12. Just as for surface codes, the phenomenological noise MLE decoder can be mapped to a random-plaquette gauge model (RPGM) on classical spins such that the zero-temperature order-disorder phase transition in the spin model corresponds to the accuracy threshold of the color codes. Because of this, as argued in Ref. [27], the mutual intersection of the curves in Fig. 12 at the threshold  $p_c$  corresponds to critical behavior in the spin model such that the spin correlation length  $\xi$  scales as

$$\xi \sim |p - p_c|^{-\nu_0}, \quad (33)$$

where  $\nu_0$  is a critical exponent set by the universality class of the spin model.

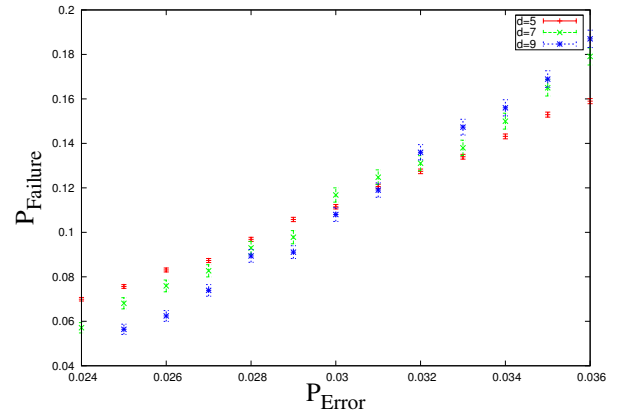


FIG. 12: Monte Carlo data used to estimate the accuracy threshold in the phenomenological noise model.



For a sufficiently large code distance  $d$ , then, the failure probability should scale as

$$p_{\text{fail}} = (p - p_c)d^{1/\nu_0}. \quad (34)$$

We use our Monte Carlo data to fit to this form, but as in Ref. [27], we allow for systematic corrections coming from finite-size effects that create a constant offset. Specifically, we use the method of differential corrections [55] to fit the curves to the form

$$p_{\text{fail}} = A + B(p - p_c)d^{1/\nu_0}. \quad (35)$$

The linear fits to our data are plotted in Fig. 13. Using the software of Ref. [55], we found the following values for  $p_c$  and  $\nu_0$ :

$$p_c = 0.030\,534 \pm 0.000\,385 \quad (36)$$

$$\nu_0 = 1.486\,681 \pm 0.166\,837. \quad (37)$$

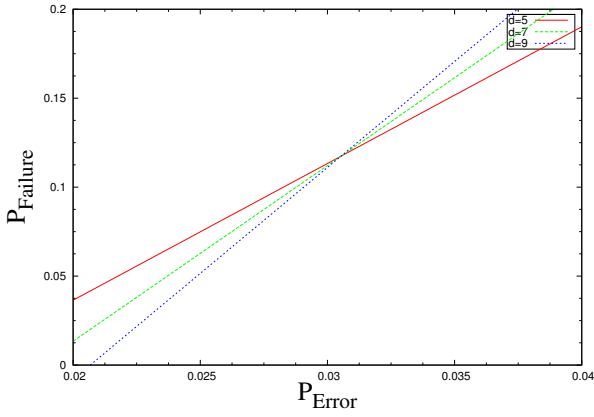


FIG. 13: Linear fit near curve crossings of phenomenological-noise-model Monte Carlo data. Estimated accuracy threshold is  $p_{th} = 3.05(4)\%$ .

To put our results in context, as we did in the code capacity setting, we reference Table I. For the same reasons as in the code capacity noise model setting, the threshold we compute is larger than the MLE decoder's threshold for the 4.4.4.4 surface codes. We conjecture that is it also measurably less than the threshold for the optimal color-code decoder, as is the case for optimal vs. MLE decoding for surface codes. So far, the threshold for optimal decoding of 4.8.8 color codes has not been estimated, but the analysis for optimal decoding of 6.6.6 color codes suggests that the threshold will be near 4.5%. If true, our data would signal a violation of the Nishimori conjecture for the RPGM associated with the 4.8.8 color code, something we are not aware of being reported elsewhere.

Finally, we note that while the value of  $\nu_0$  is consistent with value of  $\nu_0 = 1.463(6)$  obtained for the 4.4.4.4 surface code [27] and the 6.6.6 color code, the uncertainty in the value we obtained is too high to draw any meaningful conclusions.

### C. Circuit-level noise model

As with the phenomenological noise model, computing  $p_{\text{fail}}(p)$  exactly even for small code sizes is intractable, so we again appeal to Monte Carlo estimation. Our Monte Carlo simulation algorithm is similar to Algorithm 1, except the manner in which the error pattern  $E$  is generated is different. To generate  $E$ , we simulate BP and DP channel noise as described by the noise model on the explicit circuit given for syndrome extraction. This results in a correlated error model for syndrome and data qubits. We then use the phenomenological noise MLE decoder and assess success or failure as we did for that noise model.

We estimated the  $p_{\text{fail}}(p)$  curves for several small 4.8.8 triangular color codes for both the  $X$ -then- $Z$  schedule of Fig. 6 and the interleaved  $X$ - $Z$  schedule of Fig. 7. Our results are plotted in Figs. 14 and 15.

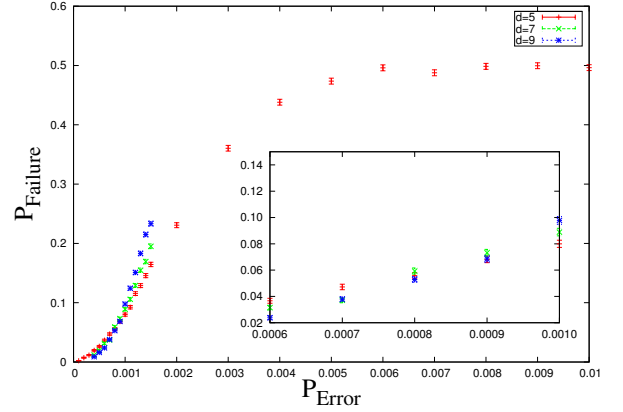


FIG. 14: Monte Carlo data used to estimate accuracy threshold in the circuit-based noise model in which the noninterleaved syndrome extraction circuit is used.

To compute the accuracy thresholds from our data, we again fit our data near the crossings to an equations whose form is similar to that of by Eq. (35). However, the motivation for such a fit is a bit more tenuous in this case because while the MLE decoder we are using maps to a RPGM, the noise model which generates it is correlated. For this reason, as also found in Ref. [27], we found it necessary to include a quadratic term, unlike the case for the pure phenomenological noise model. In other words, we fit our data to an equation of the form

$$p_{\text{fail}} = A + B(p - p_c)d^{1/\nu_0} + C(p - p_c)^2d^{2/\nu_0}. \quad (38)$$

The quadratic fits to our data for the  $X$ -then- $Z$  schedule are plotted in Fig. 16. Again using the software of Ref. [55], we found the following values for  $p_c$  and  $\nu_0$  for the  $X$ -then- $Z$  schedule:

$$p_c = 0.000\,820 \pm 0.000\,022 \quad (39)$$

$$\nu_0 = 1.350\,954 \pm 0.079\,188. \quad (40)$$

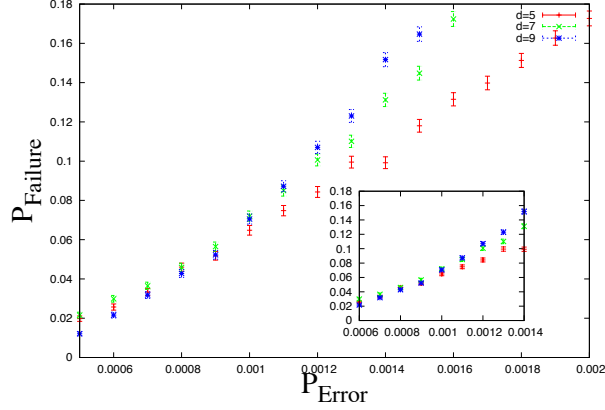


FIG. 15: Monte Carlo data used to estimate the accuracy threshold in the circuit-based noise model in which the interleaved syndrome extraction circuit is used.

To be clear, there is both a  $Z$ -error and an  $X$ -error accuracy threshold; we report the smaller of the two here.

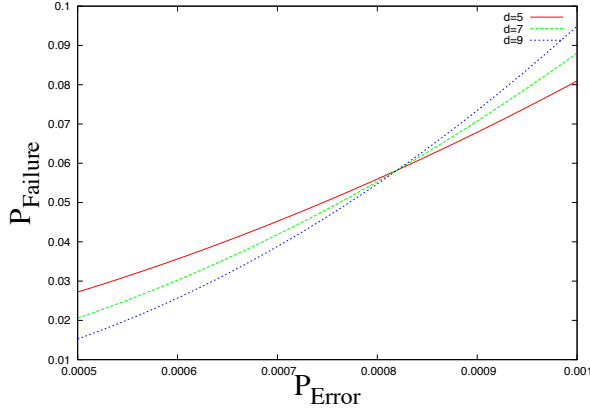


FIG. 16: Quadratic fit near curve crossings of noninterleaved-circuit circuit-based-noise-model Monte Carlo data. Estimated accuracy threshold is  $p_{th} = 0.082(3)\%$ .

Similarly, for the  $XZ$ -interleaved schedule we found

$$p_c = 0.000\,800 \pm 0.000\,037 \quad (41)$$

$$\nu_0 = 1.509\,871 \pm 0.151\,690. \quad (42)$$

To remind, our results are for the smaller of the  $X$ -error and  $Z$ -error thresholds.

Our results show that despite our efforts to shorten the schedule of the syndrome extraction circuit, the impact on the resulting accuracy threshold is essentially indistinguishable. The value of  $0.082(3)\%$  for the accuracy threshold for MLE decoding of the 4.8.8 color codes in the

circuit-level noise model is about a factor of ten less than the the corresponding  $0.68\%$  accuracy threshold for MLE decoding of 4.4.4.4 surface codes in the circuit-level noise model. We believe that the difference comes from the fact that the 4.8.8 codes have some weight-8 stabilizer generators while the 4.4.4.4 codes only have weight-4 stabilizer generators. This causes the circuits for extracting the syndrome for the weight-8 generators in the 4.8.8 codes to be larger, inviting more avenues for failure. Indeed, we have investigated the finite-sized error-propagation patterns for the 4.8.8 codes such as the one depicted in Fig. 8, and they are significantly larger and more complex than the corresponding patterns for the 4.4.4.4 surface codes. Expanding this line of reasoning, we predict that the 6.6.6 color codes will have an MLE-decoded accuracy threshold in the circuit-based noise model that is somewhere between the 4.8.8 and 4.4.4.4 accuracy thresholds in this noise model.

## V. ANALYTIC BOUND ON THE ACCURACY THRESHOLD FOR FAULT-TOLERANT QUANTUM ERROR CORRECTION

While numerical estimates of the accuracy threshold are valuable, equally valuable are analytic proofs that the accuracy threshold is no smaller than a given value. One method of obtaining such a lower bound is to use the self-avoiding walk (SAW) method, first proposed in Ref. [16]. The idea behind this method begins with the observation that our goal is to lower-bound the failure probability of decoding, which is the probability that the actual errors plus the inferred correction (modulo 2) lead to an error chain that corresponds to a logical operator. For color codes, logical operators can be not only string-like but also string-net like, as described in the original paper on color codes [20]. They must also have a Pauli-weight at least as large as the distance of the code. The probability that a logical operator is present in the post-corrected state is therefore at least as large as the probability that an error-chain string of Pauli-weight equal to the code distance is present. Certainly this is a very pessimistic bound; there are many error chain strings and string-nets of this Pauli weight that do not result in failure!

The SAW lower-bound method can be applied relatively straightforwardly to the code-capacity and phenomenological noise models with MLE decoding. The method begins to break down when applied to the circuit-level noise model with phenomenological MLE decoding. One reason for this is that the circuit introduces correlated errors, called “hooks” in Ref. [16], which suggest that the SAW bounding the failure probability should be allowed to sometimes take more than one step in a single iteration. With some finesse, this can be accounted for and bounded as in Ref. [16]. However, for the color codes, the steps need not be path-connected either. For example, the circuit may create three separated errors on a single octagon plaquette. Calling such a process

a “walk” or attempting to bound the behavior of the process by a true SAW method is dubious at best. For this reason, we have chosen to omit bounding the accuracy threshold in the circuit-level noise model and instead have bounded the accuracy threshold only for the other two noise models, as described below.

### A. Code capacity noise model

As argued by Dennis *et al.* in Ref. [16], the probability that an  $[[n, k, d]]$  topological code decoded by an error-free MLE decoder fails is upper-bounded by the probability that a self-avoiding walk creates a closed path (*i.e.*, a self-avoiding polygon or SAP) of length  $d$  or greater:

$$p_{\text{fail}} \leq \sum_{L \geq d} \text{Prob}_{\text{SAP}}(L) \quad (43)$$

$$\leq n \sum_{L \geq d} n_{\text{SAP}}(L) (4p(1-p))^{L/2}. \quad (44)$$

Self-avoiding walks on the 4.8.8 lattice have been studied, and it is known that the number of self-avoiding polygons of length  $L$  on the lattice scales asymptotically as [56]

$$n_{\text{SAP}}(L) \leq P(L) \mu_{4.8.8}^L, \quad \mu_{4.8.8} \approx 1.808\,830\,01(6), \quad (45)$$

where  $P$  is a polynomial and  $\mu_{4.8.8}$  is the so-called *connective constant* for the 4.8.8 lattice. (The value  $\mu_{4.8.8}$  has been rigorously bounded to be  $1.804\,596 \leq \mu_{4.8.8} \leq 1.829\,254$  [57, 58].) For small  $p$ , each summand in Eq. (43) is upper-bounded by the term with  $L = d$ , and the number of summands is at most a polynomial in  $d$ , so that  $p_{\text{fail}} \rightarrow 0$  as  $d \rightarrow \infty$  as long as

$$p(1-p) \leq \frac{1}{4\mu_{4.8.8}^2}. \quad (46)$$

Solving this equation for  $p$ , we find that the code capacity threshold is at least

$$p_c \geq 8.335\,745(1)\%. \quad (47)$$

Despite the crudeness of the SAW bound, it comes surprisingly close to the numerical value of 10.56(1) that we estimate in Sec. IV A.

### B. Phenomenological noise model

The SAW bound method is essentially the same as for the code capacity noise model, except now errors can happen on syndrome qubits as well as data qubits and the set of all relevant qubits forms a three-dimensional volume. The relevant SAW traverses a 3D lattice that connects syndrome qubits and data qubits both with themselves and each other as dictated by the color code; the corresponding nonregular prismatic lattice is depicted in

Fig. 17. To our knowledge, the connective constant for this lattice is not known, but it could be computed in principle using standard methods, *e.g.*, those outlined in Refs. [56–58]. We opted to bypass this analysis and instead compute a coarser bound on the failure probability.

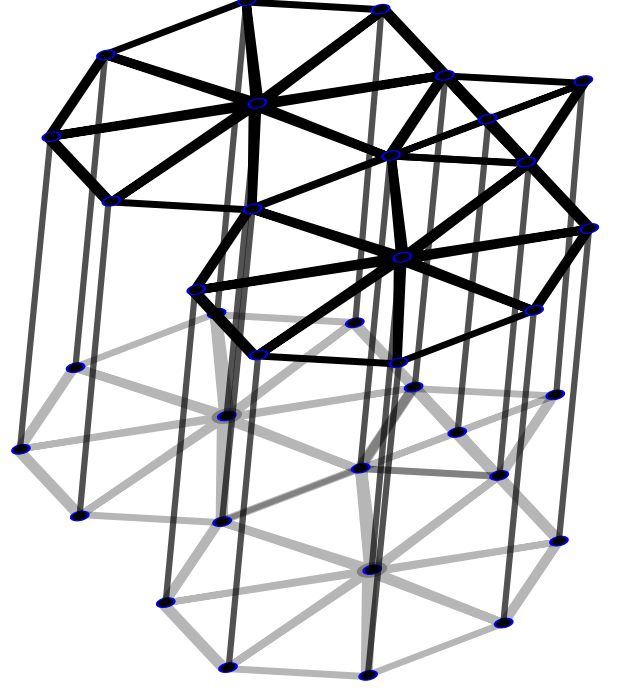


FIG. 17: Prismatic lattice on which a self-avoiding walk occurs in the analysis of the accuracy threshold for fault-tolerant quantum error correction using color codes in the phenomenological noise model.

Because the lattice in Fig. 17 has vertices of degree  $\Delta$  equal to 6, 8, and 10, we can bound the number of SAPs of length  $L$  by

$$n_{\text{SAP}}(L) \leq 2\Delta_{\text{max}}(2\Delta_{\text{max}} - 1)^{L-1}. \quad (48)$$

Using  $\Delta_{\text{max}} = 10$ , we obtain a formula similar to that of Eq. (46), namely

$$p(1-p) \leq \frac{1}{4(9)^2} = \frac{1}{324}. \quad (49)$$

Solving this equation for  $p$ , we find that the phenomenological noise threshold is at least

$$p_c \geq \frac{9 - 4\sqrt{5}}{18} \approx 0.3096\%. \quad (50)$$

This bound is nearly a factor of ten less than the value of  $p_c = 3.05(4)\%$  that we estimate in Sec. IV B. With further computational effort in determining the connective constant of the governing lattice, we suspect that the SAW bound will still be below our numerical estimate, but significantly closer, in analogy with the relationship between our SAW bound for the code capacity and the value we estimate numerically. We leave this analysis to others wishing to tighten this bound.

## VI. FAULT-TOLERANT COMPUTATION WITH COLOR CODES

To establish a threshold for fault-tolerant quantum computation, it is sufficient to establish three things: 1) a threshold for fault-tolerant quantum error correction, 2) a procedure for performing a universal set of gates in encoded form, and 3) that a failure in an encoded gate that occurs with probability  $p$  leads to failures in each output codeword with probability at most  $p$ . These three ingredients establish that each gate in a quantum circuit can be simulated fault-tolerantly by performing it in encoded form followed by fault-tolerant quantum error correction. We previously established the first criterion in Sec. III. We establish the second two criteria here for two possible computer architectures.

In the first, which we call the “pancake architecture,” each logical qubit is stored in its own triangular 4.8.8 color code and the logical qubits are stacked atop one another. This architecture is essentially the same as the one proposed in Ref. [16]. Almost all encoded operations are implemented transversally in this model, acting on single “logical qubit pancakes” or between two such “pancakes.” In the second, which we call the “defect architecture,” each logical qubit is stored as a connected collection of missing check operators, which we call a “defect,” in a single 2D 4.8.8 substrate. This architecture is essentially the same as the one proposed in Ref. [17]. Almost all encoded operations are performed in one of two ways: encoded single-qubit gates are performed by disconnecting a region containing the defect, operating transversally on the region, and reconnecting the region, while the encoded CNOT gate is performed by a sequence of local measurements that cause one defect to circulate around another.

### A. Fault-tolerance by transversal gates

In this section, we compute the threshold for fault-tolerant quantum computation with triangular 4.8.8 color codes when (almost) all encoded gates are implemented *transversally*. To remind, by calling a gate “transversal,” we mean that it acts identically on all physical qubits in a code block. For example a two-qubit transversal gate between two triangular codes acts as the same two-qubit physical gate between corresponding physical qubits in each code block. Some authors refer to this notion of transversality as *strong* transversality [59].

#### 1. Identity gate

The accuracy threshold for the identity gate is exactly the same as the accuracy threshold for fault-tolerant quantum error correction, by definition. Schematically, Fig. 18 depicts the noisy identity gate circuit.



FIG. 18: Noisy identity gate.  $BP$  indicates the action of the BP channel.

Formally, we can express the equivalence between the accuracy threshold for the identity gate and the accuracy threshold for fault-tolerant quantum error correction as

$$p_{th}^{(I)} = p_{th}^{(QEC)}. \quad (51)$$

#### 2. CNOT gate

The color codes are Calderbank-Shor-Steane (CSS) codes [47, 48], and for all such codes, the encoded controlled-NOT (*CNOT*) gate can be implemented *transversally*, namely by applying *CNOT* gates between corresponding pairs of physical qubits in two color codes. (For color codes, fewer *CNOT* gates than a fully transversal set also suffice.) Schematically, Fig. 19 depicts a noisy *CNOT* gate. Each physical *CNOT* gate propagates the BP channel on its control to the BP channel on its target and vice versa, so that the effective noise model seen by the fault-tolerant quantum error correction procedure on each code block after the encoded *CNOT* gate is the BP channel followed by the projection of the two-qubit DP channel onto a single qubit. Although the DP channel can create correlated errors between output code blocks, it will never cause a correlated error within a code block. Since our decoder treats the noise model phenomenologically, it does not account for DP-channel features such as the fact that in the DP channel a  $Y$  error is more probable than the combination of separate  $X$  and  $Z$  errors. For this reason, since half of the DP-channel errors act as a bit-flip on a given code block and half of them act as a phase-flip on a given code block, our decoder interprets the post-*CNOT* noise model as a BP channel with an effective error rate of  $p + p/2$  for bit flips and  $p + p/2$  for phase flips. This means that the accuracy threshold for the *CNOT* gate is actually  $2/3$  of the value for the identity gate. The *CNOT* gates used in an encoded *CNOT* gate must therefore meet a more stringent requirement than the identity gate to be implemented transversally fault-tolerantly. (However, the *CNOT* gates used in fault-tolerant quantum error correction still only need to meet the threshold for the encoded identity gate.)

$$p_{th}^{(CNOT)} = \frac{2}{3} p_{th}^{(I)}. \quad (52)$$

#### 3. Hadamard gate

The color codes are *strong* CSS codes, meaning that the  $X$ -type and  $Z$ -type stabilizer generators have the



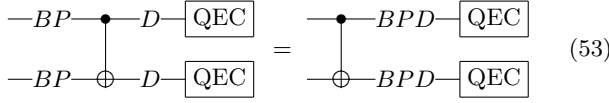


FIG. 19: Noisy *CNOT*. *BP* indicates the action of the BP channel; *D* indicates the action of the DP channel.

same structure. As with all strong CSS codes, the encoded Hadamard gate (*H*) can be implemented transversally.

Like the *CNOT* gate, the Hadamard gate propagates the BP channel to the BP channel. However, since faults in the Hadamard gate are modeled as an ideal Hadamard gate followed by the BP channel, the effective noise model is not one but *two* actions of the BP channel, as depicted in Fig. 20.

$$-BP-[H]-BP-[QEC] = -[H]-BPBP-[QEC] \quad (54)$$

FIG. 20: Noisy Hadamard *BP* indicates the action of the BP channel; *D* indicates action of the DP channel.

It is straightforward to show that two successive applications of the BP channel with probability  $p$  is equivalent to one application of BP channel with probability  $2p(1-p)$ . This is therefore the effective post-Hadamard noise channel, so that the threshold for the Hadamard gate is about half of that for fault-tolerant quantum error correction:

$$p_{th}^{(H)} = \frac{1}{2} - \frac{1}{2}\sqrt{1-2p_{th}^{(I)}} \approx \frac{1}{2}p_{th}^{(I)}. \quad (55)$$

#### 4. Phase gate

The color codes have the feature that each stabilizer generator for the code has a Pauli weight equal to 0 mod 4 and each pair of generators are incident on 0 mod 2 qubits. One can show that because of this, the encoded phase gate (*S*) has a transversal implementation [20, 60]. (Technically, it is the transversal  $S^\dagger$  operation that acts as an encoded *S*.)

While a faulty phase gate acts as an ideal phase gate followed by a BP channel, the phase gate itself does not propagate the BP channel preceding it symmetrically for bit flips and phase flips. This follows from the conjugation actions

$$SXS^\dagger = Y = iXZ \quad SZS^\dagger = Z. \quad (56)$$

The phase gate therefore propagates a phase flip to a phase flip and a bit flip to both a bit-flip and a phase flip, as depicted in Fig. 21.

The phase gate is correspondingly more sensitive to phase-flip noise because the effective phase-flip strength

$$-B-[S]-B-[QEC] = -[S]-BPB-[QEC] \quad (57)$$

$$-P-[S]-P-[QEC] = -[S]-PP-[QEC] \quad (58)$$

FIG. 21: Noisy phase gate. *B* indicates the action of the bit-flip channel; *P* indicates the action of the phase-flip channel.

is  $p^3 + 3p(1-p)^2$ . The phase gate thus has separate thresholds for bit-flip and phase-flip noise. For bit-flip noise, the threshold is

$$p_{th}^{(S, \text{bit-flip})} = \frac{1}{2} - \frac{1}{2}\sqrt{1-2p_{th}^{(I)}} \approx \frac{1}{2}p_{th}^{(I)}. \quad (59)$$

For phase-flip noise, one must solve a cubic equation to get a closed-form solution for the threshold as a function of the threshold for the identity gate. While this is possible in principle, to save space we simply state the cubic equation in the variable  $x = p_{th}^{(S, \text{phase-flip})}$  that must be solved and its approximate solution, which we can estimate because we know that the accuracy threshold is very close to 0:

$$x^3 + 3x(1-x)^2 = p_{th}^{(I)}, \quad (60)$$

$$x \approx \frac{1}{3}p_{th}^{(I)}. \quad (61)$$

#### 5. Single-qubit measurements

To *destructively* apply the encoded single-qubit measurements  $M_X$  and  $M_Z$ , we transversally measure *X* or *Z* on each of the qubits in the code block. We then perform classical error correction on the measurement outcomes (because they may be faulty) to infer the outcome of the encoded measurement, as depicted schematically in Fig. 22.

$$-B-[M_Z]-[CEC] = -[M_Z]-B-[CEC] \quad (62)$$

$$-P-[M_X]-[CEC] = -[M_X]-B-[CEC] \quad (63)$$

FIG. 22: Noisy measurements. *B* denotes the bit-flip channel, *P* denotes the phase-flip channel, and CEC denotes classical error correction of the measurement outcomes. Post-measured states are drawn with double lines to indicate that they are “classical.”

The correctness of this procedure follows from the fact that *X* and *Z* operators can be expressed as  $Z = S^2$  and  $X = HZH$ , and the encoded operations *H* and *S* have previously been demonstrated to have transversal encoded implementations. Bit or phase errors (as relevant) before a measurement then map to bit errors on the observed classical bit pattern.

The reason the measurement is destructive is that after the measurement, the qubits are no longer in the

codespace of the color code; the post-measured state is not projected onto an  $X$  or  $Z$  eigenstate in the codespace. However, as pointed out by Steane [46], given the ability to prepare encoded  $|+\rangle$  states, a circuit composed of transversal  $CNOT$  and transversal destructive  $M_X$  measurements can implement *nondestructive*  $M_X$  measurements transversally. A similar story holds for encoded  $|0\rangle$  states and  $M_Z$  measurements. The circuits for generating these nondestructive measurements transversally are depicted in Fig. 23. Because the encoded  $|0\rangle$  and  $|+\rangle$  states are being used to enable gates, namely nondestructive encoded measurements, these states are called “magic states” for the gates [61]. Ordinarily, quantum error correction would follow not just one, but both of the outputs of the encoded  $CNOT$  gate in these circuits, but because one of the encoded qubits is destructively measured immediately after the  $CNOT$  gate, that encoded qubit does not require quantum error correction; it will be effectively performed by the classical error correction process occurring after the destructive measurement.

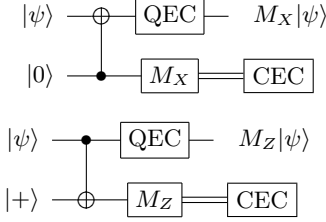


FIG. 23: Circuits for nondestructive encoded  $M_X$  and  $M_Z$ , using the states  $|0\rangle$  and  $|+\rangle$  as “magic states.”

The threshold for destructive  $M_Z$  and  $M_X$  measurements is the same as the code capacity threshold for the code, regardless of which noise model we are considering. This is because the physical measurements are made only once, as repetition cannot improve their effective error rate. The (flawless) classical error correction performed in post-processing has a threshold equal to the code capacity threshold. Hence, we have the result that

$$p_{th}^{(M_X, \text{destructive})} = p_{th}^{(I, \text{code capacity})}, \quad (64)$$

$$p_{th}^{(M_Z, \text{destructive})} = p_{th}^{(I, \text{code capacity})}. \quad (65)$$

Although these measurements need only be smaller than the code capacity threshold to implement the encoded measurement, when these measurements are used in the fault-tolerant quantum error correction protocol, they must be smaller than the threshold set by the prevailing noise model—a threshold that may be significantly lower.

To compute the threshold for nondestructive  $M_Z$  and  $M_X$  measurements, we examine how errors propagate through the circuits in Fig. 23. As with the analysis of Fig. 19, the effective noise channel we need to consider after the  $CNOT$  gate is the BP channel followed by the DP channel on each output. One of these enters a destructive measurement, which, as we found in the analysis of

Fig. 22, has a rather high threshold equal to the code capacity even in the circuit-level noise model. However, it is lowered slightly by the fact the effective error rate is  $\frac{2}{3}p$ , as discussed in the analysis of the encoded  $CNOT$  gate. The other output enters a standard quantum error correction circuit, also subject to noise of strength  $\frac{2}{3}p$ . Since the lowest threshold of these two thresholds is this one, the overall threshold for an encoded nondestructive measurement is the same as the threshold for the encoded  $CNOT$  gate. Namely, we have the result that

$$p_{th}^{(M_X, \text{nondestructive})} = p_{th}^{(CNOT)} = \frac{2}{3}p_{th}^{(I)}, \quad (66)$$

$$p_{th}^{(M_Z, \text{nondestructive})} = p_{th}^{(CNOT)} = \frac{2}{3}p_{th}^{(I)}. \quad (67)$$

## 6. $|0\rangle$ and $|+\rangle$ preparation

It is tempting to assert that the way to fault-tolerantly prepare the encoded  $|0\rangle$  state is to perform an encoded nondestructive  $M_Z$  measurement. The flaw with this reasoning is that the nondestructive  $M_Z$  measurement requires the encoded  $|+\rangle$  state as a magic state, and the analogous way of preparing a  $|+\rangle$  state requires a  $|0\rangle$  state.

To get out of this chicken-and-egg cycle, one must use an independent process. We describe a two-step process that works for preparation of an encoded  $|0\rangle$  state; the process for preparing an encoded  $|+\rangle$  state is similar.

The first step is to prepare the product state  $|0\rangle^{\otimes n}$  by transversally measuring  $M_Z$  on each physical qubit. This state is a stabilizer state, having  $n$  check operators, with check operator  $i$  being  $Z$  on qubit  $i$  for  $i = 1, \dots, n$ . The second step is to fault-tolerantly measure the  $X$  checks for the color code. Because the only  $Z$ -type operators consistent with all the  $X$  checks are the color codes’  $Z$  checks for the color code and the logical  $Z$  operator, these measurements will transform the state into the logical  $|0\rangle$  state.

It turns out that it is not necessary to also fault-tolerantly measure the  $Z$  checks for the color code. The state is already in an eigenstate of these operators at this point, so all the measurements can do is yield syndrome bits. Had one obtained these bits and processed them, the post-corrected state would still have been subject to  $X$  errors drawn from the same distribution as the  $X$  errors afflicting the initial  $|0\rangle^{\otimes n}$  preparation—fault-tolerant error correction doesn’t suppress the final error rate to zero, it only keeps it at the same rate one started with.

The threshold for preparation of encoded  $|0\rangle$  and  $|+\rangle$  states is therefore the same as the threshold for fault-tolerant quantum error correction, namely,

$$p_{th}^{(|0\rangle)} = p_{th}^{(|+\rangle)} = p_{th}^{(I)}. \quad (68)$$

It is worth noting that while the process for fault-tolerantly preparing  $|0\rangle$  and  $|+\rangle$  states is not strictly

transversal, the only nontransversal operation is fault-tolerant quantum error correction, a process that is required in addition to transversal operations in any event in order to achieve fault-tolerant quantum computation.

### 7. $T$ gate

Another gate that admits a transversal implementation with a magic state is the  $T$  gate, also called the  $\pi/8$  gate, defined as

$$T := \begin{bmatrix} 1 & 0 \\ 0 & e^{-i\pi/4} \end{bmatrix} = e^{-i\pi/8} \begin{bmatrix} e^{i\pi/8} & 0 \\ 0 & e^{-i\pi/8} \end{bmatrix}. \quad (69)$$

If we have an encoded version of the state

$$|\pi/4\rangle := TH|0\rangle \quad (70)$$

$$= \frac{1}{\sqrt{2}} (|0\rangle + e^{i\pi/4}|1\rangle), \quad (71)$$

also called  $|A\rangle$  and  $|A_{\pi/4}\rangle$  in the literature, we can implement the  $T$  gate transversally using the circuit of Fig. 24. This circuit is not a Clifford circuit, because the classically-controlled  $S$  gate is not a Clifford gate. Nevertheless, it only uses gates that we have previously shown how to implement in encoded form by purely transversal operations.

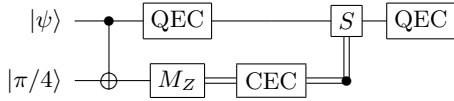


FIG. 24: Magic-state circuit for the  $T$  gate.

To compute the  $T$  gate threshold, we again study error propagation through its defining circuit, *viz.* the circuit in Fig. 24. As shown previously, the  $CNOT$  gate creates an input to the first QEC cycle that has a threshold of  $2/3$  of the standard QEC threshold. The  $S$  gate creates an input to the second QEC cycle which splits the threshold into bit-flip and phase-flip thresholds approximately equal to  $1/2$  and  $1/3$  of the standard QEC threshold. The threshold for the  $T$  gate is set by the smallest of these, namely the  $S$  gate threshold, which is

$$p_{th}^{(T, \text{bit-flip})} = \frac{1}{2} - \frac{1}{2}\sqrt{1 - 2p_{th}^{(I)}} \approx \frac{1}{2}p_{th}^{(I)}, \quad (72)$$

$$p_{th}^{(T, \text{phase-flip})} = x \approx \frac{1}{3}p_{th}^{(I)}. \quad (73)$$

### 8. $|\pi/4\rangle$ preparation

There are two alternatives for preparing encoded  $|\pi/4\rangle$  states fault-tolerantly described in the literature. In the first, low-fidelity  $|\pi/4\rangle$  states are “injected” into the code by teleportation, using the circuit in Fig. 25 [10], and

then “distilled” using encoded gates until the resultant  $|\pi/4\rangle$  states have an error below the accuracy threshold. In the second, high-quality  $|\pi/4\rangle$  states are first distilled and then injected into the code. The circuit depicted in

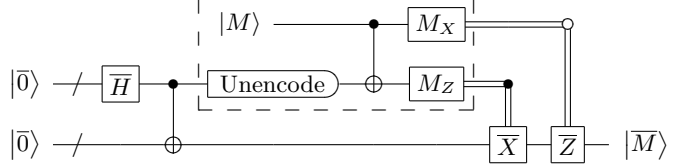


FIG. 25: Circuit for injecting a single-qubit magic state  $M$ . The circuit for multi-qubit magic states is similar.

Fig. 25 is not fault-tolerant, but faults are already suppressed by the code on the encoded qubits; only operations from the latter-half of the decoding circuit onwards are unprotected.

Unlike all of the previous encoded gates, this method for implementing an encoded  $|\pi/4\rangle$  preparation requires an operation which is neither transversal nor fault-tolerant quantum error correction. The “unencoding” portion of the circuit is the time-reversed coherent circuit for encoding a state in the color code, derivable via standard stabilizer codes as shown in Ref. [50]. This unencoding circuit does not appear to have a transversal implementation. While the Eastin-Knill theorem [62] asserts that at least one nontransversal operation is required to generate a universal set of encoded gates, it does not guarantee that no transversal implementation of this circuit exists. That is because the process of fault-tolerant quantum error correction used to prepare  $|0\rangle$  and  $|+\rangle$  states is not transversal. For 3D color codes [63], in which  $T$  is intrinsically transversal and in which encoded  $|0\rangle$  and  $|+\rangle$  states still require fault-tolerant quantum error correction for preparation, only transversal and FTQEC operations are needed, for example. It would be interesting to develop a variant of the circuit in Fig. 25 which only uses transversal operations and possibly fault-tolerant quantum error correction to inject a  $|\pi/4\rangle$  state into 2D color codes. We leave that for others to explore.

While the portion of the circuit in Fig. 25 in which the physical  $|M\rangle$  state interacts with the unencoded qubit via a  $CNOT$  appears to also not be transversal, it can be made so with slight modification. In principle, one could prepare  $n$  states of the form  $|M\rangle$  and transversally apply the  $CNOT$  gate between these and the code block, but only the one qubit corresponding to the unencoded state will be used to classically control the  $\bar{X}$  and  $\bar{Z}$  gates that are used to inject the correct state. As usual, these corrections do not need to be actually implemented, only used to update the Pauli frame.

Both alternatives for preparing high-quality encoded  $|\pi/4\rangle$  states require a procedure for magic-state distillation. One option is to use the encoding circuit for the 15-qubit Reed-Muller code [6] (also the smallest 3D color code [63]) run in reverse, as depicted in Fig. 26. For it to work, the initial states must have an error less

than the  $|\pi/4\rangle$  distillation threshold. For the circuit depicted in Fig. 26, the distillation threshold for independent, identically distributed (iid) depolarizing noise is  $(6 - 2\sqrt{2})/7 \approx 45.3\%$  [64, 65], for dephasing iid noise is  $(\sqrt{2} - 1)/\sqrt{2} \approx 29.3\%$  [64, 66], and for worst-case iid noise is  $(\sqrt{2} - 1)/2\sqrt{2} \approx 14.6\%$  [64, 66]. The entire circuit must be run  $\mathcal{O}(\text{poly}(\varepsilon^{-1}))$  times to achieve an output error less than  $\varepsilon$ ; convergence should be quite rapid in practice given the actual polynomial [64]. Various tricks can be used to boost the distillation threshold and reduce the resources required to achieve high-fidelity states; any of these can be readily adapted to this setting.

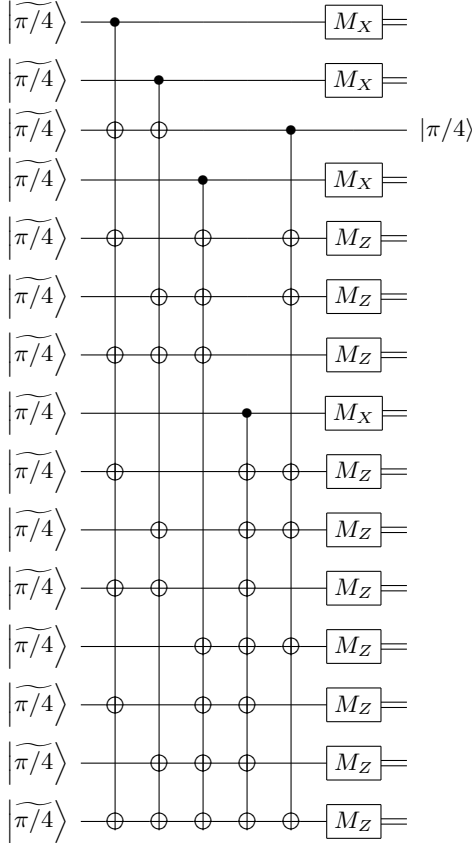


FIG. 26: Distillation circuit for  $|\pi/4\rangle$  states; it is the 15-qubit Reed-Muller code’s encoding circuit in reverse.

### 9. Synthesis

It is well-known result the gate basis  $\{H, S, CNOT, M_X, M_Z, |0\rangle, |+\rangle, |\pi/4\rangle\}$  is universal for quantum computation [36] (in fact, it is even over-complete). We have presented transversal methods for performing color-code encoded versions of each of these except for the state preparations. By the Eastin-Knill theorem [62], it is impossible to generate a complete universal encoded gate basis in transversal form. However, color codes offer a particularly gentle way around this theorem. There are only two nontransversal operations

used. The first is fault-tolerant quantum error correction, a process that is required in addition to encoded computations in any event for the entire protocol to be fault tolerant. The second is the time-reversed coherent encoding circuit for color codes. Such a circuit is useful for encoding unknown quantum states, but in an actual quantum computation, the input state is known so it is not needed for this purpose. Whether this “unencoding circuit” can be replaced with another operation which uses only transversal operations and fault-tolerant quantum error correction is an interesting open question. For 3D color codes, we know that the answer is “yes.”

The “pancake architecture,” described in Ref. [16] for the Kitaev surface-codes, realizes the encoded gate set we described using only gates between spatially neighboring qubits. One difference in our analysis from that performed in Ref. [16] is that we have analyzed the accuracy threshold not only for fault-tolerant quantum memory but also for fault-tolerant quantum computation, a feat made tractable by the strong CSS nature of the color codes.

### B. Fault-tolerance by code deformation

The method of fault-tolerance described in Sec. VIA requires a three-dimensional architecture to allow the transversal *CNOT* gates to remain spatially local. This violates the spirit of using two-dimensional codes in the first place. Fortunately, it is possible to use *code deformation* to achieve fault-tolerance in a strictly two-dimensional architecture. Our construction here mirrors that of Raussendorf *et al.*’s construction for surface codes [17, 67]. Fowler has independently constructed a method for using code deformation in 4.8.8 color codes that is similar to ours [49]. Some salient differences between our method and Fowler’s are that (i) Fowler’s logical qubits are always encoded in a triple of defects whereas ours are encoded in single defects except during certain logical gates, and (ii) Fowler’s scheme disallows different defect types from occupying the same plaquette location while ours does not. Each of these differences allows our scheme to encode a higher density of information. Specifically, our scheme allows a six-fold increase in logical qubit density over the Fowler scheme.

To begin, we generate a sufficiently large 4.8.8 triangular color code by performing fault-tolerant quantum error correction on a collection of qubits. We are not interested in what state the triangular code encodes—all we require is that the state is in the codespace with arbitrarily high fidelity. We consider any logical qubits associated with the entire surface to be “gauge” qubits in the language of subsystem stabilizer code theory [68]. We will use this state as a substrate for generating and manipulating encoded qubits.

Each element of the standard set of stabilizer generators for a color code can be labeled by a face of a definite



color (red, green, or blue) and an operator of a definite Pauli type ( $X$  or  $Z$ ). Notationally, we will refer to a generator as a  $(c, P)$  generator if it is of color  $c$  and Pauli type  $P$ . To prepare an encoded qubit in our color code substrate, we remove a connected product of stabilizer generators of the same color and type. (Generally removal of any element of the stabilizer group will yield a logical qubit; we restrict attention to this class for simplicity.) We call this removed region a *defect* in analogy with the language used by Raussendorf *et al.* in Ref. [17]. This removal is entirely passive—we simply cease measuring this product of stabilizer generators in future quantum error correction rounds. For this reason, it is manifestly a fault-tolerant process.

In the following sections, we describe how to perform a universal repertoire of encoded logic gates on defect-based logical qubits, with arbitrarily high fidelity. This is therefore a prescription for fault-tolerant quantum computation using code deformation.

### 1. Preparing a defect in $|0\rangle$ or $|+\rangle$

In principle, the generator removed to form a defect qubit can be identified with any element of the encoded Pauli group for that encoded qubit. For concreteness, we make the choice of calling the removed generator a logical  $Z$  when it is  $Z$ -type defect (also called a ‘primal’ or ‘smooth’ defect in the language of Ref. [17]) and a logical  $X$  when it is  $X$ -type defect (also called a ‘dual’ or ‘rough’ defect in the language of Ref. [17]). Thus removing a  $c$ -colored  $X$ - or  $Z$ -type generator corresponds to preparing a logical  $|+\rangle_{(c,X)}$  or  $|0\rangle_{(c,Z)}$  state respectively.

The logical  $Z$  operator for a  $(c, X)$  defect acts as  $Z$  on a  $c$ -colored chain of qubits connecting the defect to another  $c$ -colored boundary, which may itself be another defect. If no such other boundary exists, then the defect fails to encode a logical qubit. To avoid this complication, we have chosen our substrate to be a triangular code, having boundaries of each of the three colors. Similarly, the logical  $X$  operator for a  $(c, Z)$  defect acts as  $X$  on a  $c$ -colored chain of qubits connecting the defect to a  $c$ -colored boundary.

Preparing a  $|+\rangle_{(c,Z)}$  or  $|0\rangle_{(c,X)}$  state requires more care. To do this, we measure  $M_X$  or  $M_Z$  respectively along a  $c$ -colored chain of qubits from the plaquette we wish to store the logical qubit in and the nearest  $c$ -colored boundary. This projects each qubit along the chain into either  $|+\rangle$  or  $|-\rangle$  (resp.  $|0\rangle$  or  $|1\rangle$ ), which we can interpret as  $|+\rangle$  (resp.  $|0\rangle$ ) for each qubit by changing local Pauli bases. We then measure the  $Z$ -checks (resp.  $X$ -checks) incident on this chain except the one at the defect location and correct any errors, which places the defect back into the substrate in the desired state.

An arbitrarily large  $c$ -colored defect can be prepared in a single step by ceasing to measure a collection of  $c$ -connected defects by a similar process, enabling the preparation process to be made arbitrarily reliable. This

introduces a number of ‘gauge’ qubits in the interior of the defect that can be ignored; the details of this are described in the next section.

### 2. Growing, shrinking, and moving defects

We grow a  $(c, P)$  defect qubit on region  $q$  in the following way. Suppose we would like to extend the defect so that it includes an adjacent region  $q'$  of the same color and type. (By adjacent, we mean that the regions can be connected by a single two-qubit  $c$ -colored link.) To do this, we first perform the following conditional operation. If  $P = X$ , then we measure  $ZZ$  on a  $c$ -colored link connecting the regions, while if  $P = Z$ , then we measure  $XX$  on a  $c$ -colored link connecting the regions. Examples of how this works for octagonal and square defects are depicted in Figs. 27 and 28; the circuit in Fig. 29 implements this transformation. A  $YY$  operator can be used to grow a  $X$  and  $Z$ -type defect at the same time.

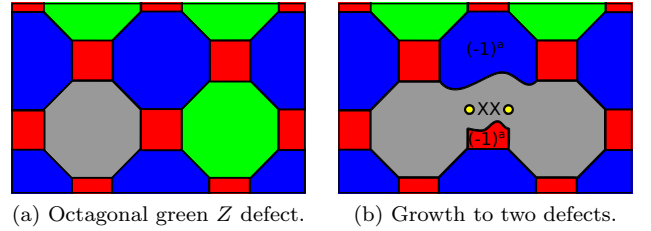


FIG. 27: Growth of an octagonal green  $Z$  defect by one site.

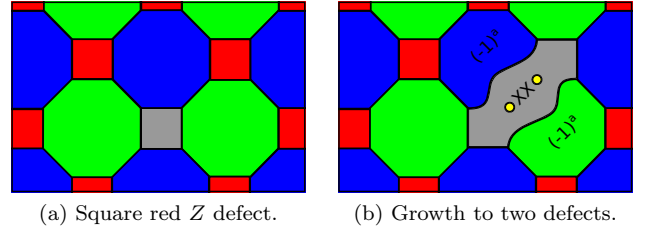


FIG. 28: Growth of a square red  $Z$  defect by one site.

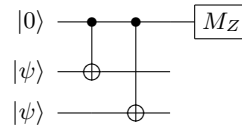


FIG. 29: Measurement of  $XX$  to grow a  $Z$ -type defect. The measurement can be performed with existing circuitry already in place for syndrome extraction.

After this measurement, the new collective defect operator is the product of the  $q$  and  $q'$  defect operators. The  $\pm XX$  or  $\pm ZZ$  operator has also been added to the list of stabilizer generators. As usual, we do not need to actually correct the result to a  $+1$  outcome: it suffices

to update the Pauli frames of the stabilizer generators incident on these two interior qubits.

Because we will no longer use the weight-two operator, we may consider it to also be a “gauge” operator in the language of subsystem stabilizer codes [68]. This also makes its anticommuting partner a gauge operator, which we may interpret to be either of the original defect operators (on  $q$  or  $q'$ ). By introducing these two new gauge operators, we may reinterpret the defect logical operator on the collective  $q$  and  $q'$  region as acting solely on its boundary. In particular, the interior of the collective  $q$  and  $q'$  region need never be involved in future syndrome extractions.

An important question is whether the defect growth process is fault-tolerant. The simplest circuit for measuring  $XX$  or  $ZZ$  would perform  $CNOT$  gates into or out of an ancilla qubit to each of the two relevant qubits, as depicted in Fig. 29. Although a single error in this ancilla qubit could propagate to two errors on the two interior qubits, because we subsequently treat these qubits as encoding a gauge qubit, we do not worry about errors on these. It could still be the case that the value of the measurement obtained is incorrect, which impacts the update of the Pauli frame of the two adjacent stabilizer generators in a correlated way. Thus a single syndrome measurement error would propagate to two syndrome-bit errors. To prevent this happening to first order in the error probability, we repeat the  $XX$  or  $ZZ$  measurement twice and use the majority vote of the three outcomes to update the Pauli frame.

Compared to the process of defect growth, defect contraction is much simpler: to shrink a defect by a single-plaquette, one simply measures that plaquette operator in the next round of fault-tolerant quantum error correction.

By a combination of local growth and shrinking processes, one can deform the code with a  $(c, P)$  defect at one plaquette to a code with a  $(c, P)$  defect anywhere else. In other words, the *move* operation for a defect can be decomposed into a sequence of more elementary *grow* and *shrink* operations.

### 3. Measuring a defect

To destructively measure the logical operator encircling a defect, one first shrinks the defect to size of a single plaquette. Then one measures the defect with the existing circuitry at that plaquette as though it were a local stabilizer generator. The shrunken defect will have a significantly lower tolerance to one type of Pauli error but that error type is in the basis being measured in and will not disturb the measurement outcome. To destructively measure the string-like logical operator connecting two defects, one brings the two operators as close together as possible. One then measures the weight-two operator connecting the defects using the circuitry used to grow a defect from one site to encompass the other. Again, the

tolerance to errors of one Pauli type will be significantly lower, but this will not be of the type that disturbs the measurement.

To nondestructively measure a defect, one uses the circuit of Fig. 23, which uses destructive measurement of  $M_Z$  or  $M_X$ , preparation of  $|0\rangle$  or  $|+\rangle$ , and the  $CNOT$  gate described in the next section.

### 4. $CNOT$ gate between defects

It is straightforward to show that moving a  $(c, Z)$  defect qubit around a  $(c', X)$  defect qubit (or vice-versa) generates an encoded  $CNOT$  gate controlled by the  $(c, Z)$  defect when  $c$  and  $c'$  are different colors; the construction is essentially the same as that in Refs. [17, 49, 67]. Since this process traces out a braid in spacetime, we call this process “braiding defects.” Also drawing upon Refs. [17, 67], one can generate a  $CNOT$  gate between two  $Z$ -type defects or two  $X$ -type defects, whether they are the same color or not. The circuit for doing this between two  $Z$ -type defects is depicted in Fig. 30; the circuit for doing this between two  $X$ -type defects is similar.

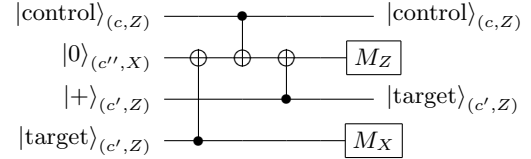


FIG. 30: Circuit for braiding a  $CNOT$  gate between  $Z$ -type defects. The colors  $c$  and  $c'$  may be the same or different, but the color  $c''$  is a color different from these. The circuit for braiding a  $CNOT$  gate between  $X$ -type defects is similar: the  $CNOT$  gate directions are reversed, the types of the defects and the types of the measurements have their Pauli types swapped from  $X$  to  $Z$  and vice-versa, and the  $|0\rangle$  state becomes a  $|+\rangle$  state and vice-versa.

One can convert an  $X$ -type defect into a  $Z$ -type defect, or vice-versa, (changing its color as a side effect) using one of the circuits in Fig. 31. In conjunction with the other type of  $CNOT$  gates mentioned, this allows  $CNOT$  gates between two defects regardless of the colors or Pauli types they have.

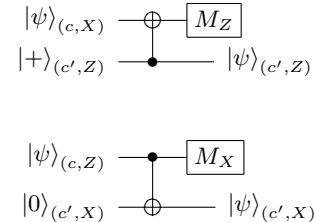


FIG. 31: Circuits for converting a  $Z$ -type defect into an  $X$ -type defect and vice-versa.

### 5. Phase gate on a defect

To perform an  $S$  (phase) gate on a  $(c, P)$  defect, we prepare two more qubits of  $(c', P)$  and  $(c'', P)$  type, each in the state  $|0\rangle$  and use  $CNOT$  gates to put the defect into a three-defect repetition code. This maps our single-defect logical qubits into the three-defect logical qubits Fowler uses in his construction [49]. We then grow the defects and connect them so that they separate an interior triangular region from an exterior region, just as described in Fowler’s construction. If  $P = Z$ , then as Fowler noted, it suffices to apply  $S$  transversally (actually,  $S^\dagger$  must be applied transversally) to generate a logical  $S$  on the triple-defect qubit. However, if  $P = X$ , then Fowler’s construction fails, because the “exterior trees” in his language fail to undergo the action  $SXS^\dagger = Y$ . “Pruning” the exterior tree as Fowler suggests for his implementation of the Hadamard gate fails as well, because such an operation yields only the “byproduct operator” for logical  $X$  or  $Z$  on the triple-defect qubit, but not both. To perform the  $S$  gate on  $X$ -type defects, we propose the following two-step procedure. First, we arrange the defects to separate a triangular interior from the exterior and apply  $S^\dagger$  transversally on the interior. Second, we rearrange the defects so that part of what was the exterior becomes the new interior, and perform  $S^\dagger$  transversally on this new triangular interior. In this way, both the interior and exterior trees experience the  $S$  gate. Once the gate is complete, we run the three-defect encoding circuit in reverse and absorb the two ancilla qubit regions back into the substrate in subsequent quantum error correction rounds.

Of course, the  $S$  gate can also be achieved via magic states of the form  $|\pi/2\rangle := \frac{1}{\sqrt{2}}(|0\rangle + e^{i\pi/2}|1\rangle)$  (also called  $|Y\rangle$  or  $|+\hat{i}\rangle$  in the literature) in a manner similar to what is done for surface codes. But this is one of the great benefits of 4.8.8 color codes—no magic state distillation and usage is required to realize this gate in encoded form. It may well be worth the lower accuracy threshold of color codes relative to surface codes in order to achieve the resource reduction for performing encoded  $S$  gates.

### 6. Hadamard gate on a defect

From one point of view, a logical Hadamard gate is unnecessary because it can be implemented using the gates we have previously described, for example by the circuit of Fig. 32. However, we have developed a more resource-

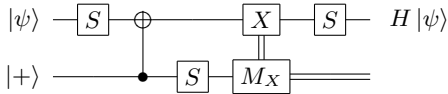


FIG. 32: Circuit for simulating  $H$  with previously-described gates.

efficient way to perform this gate that we describe here.

If we want to perform a Hadamard gate on a  $(c, P)$  defect, we first prepare an ancillary  $(c, P)$  defect in the state  $|0\rangle$  and perform a  $CNOT$  gate from the defect qubit to this defect ancilla using the circuit of Fig. 30. This encodes the original defect qubit into the two-qubit bit-flip repetition code across the two defects. The  $ZZ$  operator for the two defect qubits is in the stabilizer group of this repetition code, so we can measure  $ZZ$  without disturbing the encoded qubit. The logical  $Z$  operator is a  $c'$ -colored chain of  $Z$  operators around either of the defects and the logical  $X$  operator is a  $c$ -colored chain of  $X$  operators connecting the defects, where  $c' \neq c$ . This encoding is the one used at all times in the Raussendorf *et al.* scheme [17, 67], but here we only use it to perform the Hadamard gate and go back to our original single-defect encoding once the gate is completed.

After we’ve encoded the defect qubit into two, we then perform individual  $M_Z$  measurements on a  $c'$ -colored chain of qubits surrounding both defects, where  $c' \neq c$ . This separates the region of the two qubits from the substrate, so we can then apply  $H$  transversally on the cut-out region without influencing the external substrate. This operation applies a logical Hadamard gate to the two defect qubits in the interior, but also turns them into  $P'$ -type defect qubits in the process, where  $P'$  is conjugate to  $P$  (i.e.,  $P' = Z$  if  $P = X$ , and  $P' = X$  if  $P = Z$ ). We then stitch the cut out region back into the code by measuring the  $P$ -check operators incident on the cut. The encoding circuit for the repetition code is run in reverse, and the resulting defect can be converted back to its original type and color using circuits of the form depicted in Fig. 31.

### 7. Injecting $|\pi/4\rangle$ into a defect

To perform universal encoded quantum computation with defects, our approach requires defects encoded into the state  $|\pi/4\rangle$  with an error below its distillation threshold, as discussed in the previous “pancake” architecture. We therefore need a method for injecting magic states into defects such that the injection process introduces errors at a rate below the distillation threshold. The single-qubit preparation threshold for a magic state is therefore the difference between its distillation threshold and the error introduced by its injection process.

It is worth remarking that this kind of injection process is used in defect-based surface code schemes as well [17, 49, 69]. In these schemes, one must not only inject  $|\pi/4\rangle$  states, but also inject  $|\pi/2\rangle$  states as well. However, the impact of errors introduced by errant injection has not been studied to our knowledge. It is unclear whether considering it will significantly alter the high threshold values numerically estimated for surface codes—the difference between a 1% accuracy threshold and a 14% distillation threshold is not that great, so it is reasonable to expect that it may be quite important, especially because injection generates small-sized defects

that are not arbitrarily well-protected from noise at first. We do not investigate the impact of the injection process on the threshold for color codes here either, but we expect that it will be less consequential because the value of the color-code accuracy threshold is much lower than that for the surface codes.

To inject into a  $(c, Z)$  defect, we identify the corner of the triangular substrate containing the  $c$ -colored plaquette and measure  $M_Z$  on the qubit in the corner, isolating it from the code. We then apply  $TH$  to the corner qubit and then measure the weight-four  $X$  check in the corner, bringing the corner qubit back into the code. We then cease measuring the  $Z$  check in the standard way, creating a single-plaquette  $Z$ -type defect in the corner. This defect is not well protected from noise, so we move it from the corner and grow it as fast as we can, so that the ambient noise doesn't degrade the fidelity of the encoded state.

### 8. $T$ gate on a defect

Given  $|\pi/4\rangle$  defect qubits, we can distill them and use them to perform the  $T$  gate in the same way as described in Secs. VI A 7 and VI A 8 for the “pancake” architecture.

## VII. CONCLUSIONS

### A. Fault-tolerant quantum computation

We studied fault-tolerant quantum computation using color codes, inspired by (a) the need to minimize qubit transport in real technologies having 2D layouts and (b) the high accuracy thresholds reported for similar topological codes. We framed our study with a well-defined quantum control model and three physically-motivated noise models of increasing realism which we call the code-capacity noise model, the phenomenological noise model, and the circuit-based noise model.

The strategy behind our study was to first understand how to fault-tolerantly simulate the identity gate via fault-tolerant quantum error correction and then extend this understanding to how to fault-tolerantly simulate a universal set of quantum gates capable of general-purpose quantum computation.

In the course of studying fault-tolerant quantum error correction, we formulated most-likely-error decoding for color codes as a mathematical optimization problem known as an integer program. We also developed feasible schedules for parallelized syndrome extraction for the most efficient family of color codes, the 4.8.8 color codes. To better understand the performance of our decoder, we elaborated a previously-established connection between the performance of our decoder and some statistical-mechanical classical spin models.

Our numerically-estimated value for most-likely-error fault-tolerant quantum error correction for 4.8.8 color

codes in the code-capacity noise model is 10.56(1)%. This is not significantly different from what had previously been estimated for optimal decoding of these and the 6.6.6 color codes, or most-likely-error or optimal decoding of Kitaev's 4.4.4.4 surface codes. Indeed, the upper bound for any CSS code is slightly more than 11%, so all of these codes perform close to optimally in this noise model. To support our numerical estimate, we proved that the threshold is at least 8.335 745 (1)% using a self-avoiding walk technique.

Our numerically-estimated value for the accuracy threshold of most-likely-error fault-tolerant quantum error correction for 4.8.8 color codes in the phenomenological noise model is 3.05(4)%. Again, this is not significantly different from what had previously been estimated for optimal decoding of the 6.6.6 color codes, or most-likely-error or optimal decoding of Kitaev's 4.4.4.4 surface codes. We attribute the nominal improvement we find relative to Kitaev's surface codes for both this and the previous noise model to the fact that the color codes have higher-weight stabilizer generators, which should be modeled as more errant, but which aren't in these noise models. To support our numerical estimate, we proved that the threshold is at least 0.3096% using a self-avoiding walk technique.

Our numerically-estimated value for most-likely-error fault-tolerant quantum error correction for 4.8.8 color codes in the circuit-based noise model is 0.082(3)%. By attempting to optimize the syndrome extraction circuit by hand, we ended up surprisingly *decreasing* our threshold estimate to 0.080(3)%, suggesting that optimizing the syndrome extraction circuit to find the highest threshold is a nontrivial task. Unlike our findings for the previous two noise models, our accuracy-threshold estimate is in fact significantly different from what had previously been estimated for most-likely-error decoding of Kitaev's 4.4.4.4 surface codes—it is nearly a tenth the comparable value of 0.68%. That said, it is consistent with the value of “about 0.1%” estimated using a different suboptimal decoder for these codes considered in Ref. [22]. However, the estimate in Ref. [22] lacked any error analysis, so it is hard to determine how consistent these results truly are. We believe that the reduction in threshold relative to the surface code threshold comes from the increased weight of the stabilizer generators for the 4.8.8 color code. Based on this, we predict that the 6.6.6 color codes will have a quantum error-correction accuracy threshold for this noise model somewhere between 0.082(3)% and 0.68% without any additional optimizations. We did not prove a lower bound on the threshold in this noise model, as the self-avoiding walk technique breaks down for this noise model.

To extend our results to general-purpose fault-tolerant quantum computing, we considered two different approaches. In the first, the architecture consisted of 2D surfaces stacked like pancakes in which each surface corresponded to a logical qubit and almost all operations were either global transversal operations or local syn-



drome extraction operations. In the second, the architecture consisted of an extended 2D surface in which logical qubits were associated with “defects” and almost all operations were either defect braiding by local measurements or local syndrome extraction operations.

In the “pancake” architecture, we showed that encoded universal quantum computation was possible using only local stabilizer measurements, global transversal operations, and the time-reversed coherent encoding circuit for the color code, which was used to inject magic states. Each gate in this architecture has its own accuracy threshold that is a significant fraction of the quantum error correction (memory) threshold.

In the “defect” architecture, we showed that encoded universal quantum computation was possible using only local stabilizer measurements, code deformation, and transversal operations on isolated regions. These deformations came in different forms, including growing small defects into large ones, braiding defects around each other for encoded  $CNOT$  gates, and isolating defects from the rest of the code. Each gate has the same accuracy threshold as the quantum error correction (memory) threshold, although errors afflicting injected magic state defects before they are grown to full size may dominate the threshold for the less realistic code-capacity and phenomenological noise models.

Because the defect architecture has a higher threshold and is more consistent with the original motivation for our study—namely that many technologies are restricted to a single 2D layout—we believe the defect-based approach to be the most practical. To that end, we extended some of the defect-based approach for color codes presented in Ref. [49] so that a significantly higher density of defects can be stored and processed in the surface.

### B. Relation to statistical-mechanical phase transitions

It has been previously established that there is a mapping between quantum color codes and a classical statistical-mechanical model known as the three-body random-bond Ising model (3BRBIM). In this mapping, each check maps to a classical  $\pm 1$  spin and each qubit maps to a three-body interaction, with the interaction being ferromagnetic if the qubit is not in error and anti-ferromagnetic if it is. Specifically, the Hamiltonian constructed by this mapping is

$$H = \sum_{\text{qubits } q} J_q \prod_{\text{checks } c \ni q} S_c, \quad (74)$$

where  $J_q \in \pm 1$  indicates a flip on qubit  $q$  and  $S_c \in \pm 1$  indicates the eigenvalue of the check  $c$ .

A feature of the mapping is that the code capacity for any particular decoding algorithm represents a point on the boundary of the order-disorder transition of the associated 3BRBIM. Our integer-programming decoder is

an “energy-minimizing” decoder in this paradigm, corresponding to the phase boundary at zero temperature. Because our code-capacity value of 10.56(1)% is lower than the code capacity of 10.925(5)% of a “free-energy-minimizing” decoder implicitly explored by Ohzeki [25], this demonstrates that the phase boundary of the 3BRBIM is “re-entrant” as depicted in Fig. 11, violating the so-called Nishimori conjecture for this system. This result is counterintuitive because it states that the 3BRBIM can become *more* ordered by increasing the temperature, depending on the system’s quenched disorder parameter. It would be exciting to see experimental confirmation of this effect.

### C. Future directions

While we have been able to answer many questions about fault-tolerant quantum computing using color codes, practicalities have necessarily limited the focus of our analysis, leaving other related questions open. Our results also raise new questions that we believe are worthy of study.

One future direction we mentioned is optimizing the syndrome extraction circuit. One could also examine using more elaborate ancilla states in the circuit, such as those used in the schemes proposed by Shor [1], Steane [46], and Knill [10]. In any scheme one chooses, further improvement may still be possible by transforming the circuit used in an implementation.

Another future direction we alluded to is optimizing the decoding algorithm. One could examine the performance of the truly optimal decoder for the circuit model which accounts for the correlations in the noise induced by the syndrome extraction circuit. This will yield an upper bound on the accuracy threshold for the noise model(s) studied. On the other end of the spectrum, it would be useful to explore the performance of faster decoders which don’t yield as high a threshold as the MLE decoder but which may be more valuable in practice. The renormalization group decoder [70] and minimum-weight perfect matching decoder [16] (using a mapping of one color code to two Kitaev surface codes [24]) are examples of this. Another alternative is to generalize the results of Feldman *et al.*, who developed an efficient linear-program decoder for binary codes based on an integer-program-based decoder similar to the one we developed here [71].

The lower bound technique of self-avoiding walks that we used is certainly not the tightest, and it may be of interest to establish tighter lower bounds. For tighter bounds, it may be possible to use different techniques. In the case of the circuit-based noise model, the self-avoiding walk bound technique breaks down dramatically, and it would be worth exploring other lower-bound techniques in this setting.

While we believe the noise and control model that we studied is reasonable, it is certainly not unique and can

be improved upon with more experimental input. As shown by Levy *et al.*, [34, 35], when more realistic models are included, conclusions regarding fault tolerance can change dramatically. Even at an abstract level, one could modify our depolarizing noise model for *CNOT* gates so that it acted ideally with probability  $1-p$  and applied one of the fifteen nontrivial Pauli operators with probability  $p/15$  each rather than acting ideally with probability  $1-p$  and applying one of the sixteen Pauli operators with probability  $p/16$ .

While we gave a prescription for injecting magic states into the color code for both the pancake and 2D defect-based architectures, we did not carefully study the threshold of the circuits used for injection. To our knowledge, this type of study has not been performed for Kitaev's surface codes either. Such studies would be valuable, as it could be the case that the magic state preparation threshold is actually less than the accuracy threshold reported for all of the other gates, even though the distillation threshold for the magic states is higher than the accuracy threshold for the other gates.

Finally, the connection between color codes and the three-body random-bond Ising model allowed us to explore the structure of order-disorder transition in the latter model by studying the former. This is one of the rare examples where a purely quantum information theoretic result has led to greater understanding of a classical system. Kitaev's surface codes and the two-body random-bond Ising model have a similar connection and have admitted a similar study [16, 27]. It is clear that it is the CSS structure of these codes that admits these studies; one could argue that every CSS code is a topological

code for some topology, having an associated classical statistical-mechanical model for a given quantum noise model. It might be interesting to use the fault-tolerant decoding of CSS codes generally as a tool to explore related statistical-mechanical systems with quenched disorder.

## Acknowledgments

We would like to thank the following individuals for helpful discussions: Hector Bombin, Bob Carr, Chris Cesare, Guillaume Duclos-Cianci, Bryan Eastin, Austin Fowler, Anand Ganti, Peter Groszkowski, Jim Harrington, Charles Hill, Lloyd Hollenberg, Uzoma Onunkwo, Cindy Phillips, David Poulin, Robert Raussendorf, and David Wang. We would also like to thank Dave Gay for use of AMPL mathematical programming language. PRR was supported by the Quantum Institute at Los Alamos National Laboratories. AJL and JTA were supported in part by the National Science Foundation through Grant 0829944. JTA and AJL were supported in part by the Laboratory Directed Research and Development program at Sandia National Laboratories. Sandia National Laboratories is a multi-program laboratory managed and operated by Sandia Corporation, a wholly owned subsidiary of Lockheed Martin Corporation, for the U.S. Department of Energy's National Nuclear Security Administration under contract DE-AC04-94AL85000.

- 
- [1] P. W. Shor, *Fault-tolerant quantum computation*, in *Proceedings of the 37th Annual Symposium on Foundations of Computer Science*, edited by R. S. Sipple, IEEE (IEEE Press, Los Alamitos, CA, 14–16 Oct. 1996, Burlington, VT, USA, 1996), pp. 56–65, ISBN 0-8186-7594-2, [doi:10.1137/S0097539795293172](https://doi.org/10.1137/S0097539795293172), [arXiv:quant-ph/9605011](https://arxiv.org/abs/quant-ph/9605011).
  - [2] D. Aharonov and M. Ben-Or, *Fault tolerant quantum computation with constant error*, in *Proceedings of the Twenty-Ninth Annual ACM Symposium on the Theory of Computing*, edited by F. T. Leighton and P. Shor (ACM Press, New York, El Paso, TX, USA, 1997), pp. 176–188, ISBN 0-89791-888-6, See also extended version [3], [doi:10.1145/258533.258579](https://doi.org/10.1145/258533.258579), [arXiv:quant-ph/9611025](https://arxiv.org/abs/quant-ph/9611025).
  - [3] D. Aharonov and M. Ben-Or, *Fault tolerant quantum computation with constant error rate* (1999), See also condensed version [2], [arXiv:quant-ph/9906129](https://arxiv.org/abs/quant-ph/9906129).
  - [4] A. Y. Kitaev, *Quantum computations: algorithms and error correction*, Russian Math. Surveys **52**, 1191 (1997), [doi:10.1070/RM1997v052n06ABEH002155](https://doi.org/10.1070/RM1997v052n06ABEH002155).
  - [5] A. M. Steane, *Active stabilization, quantum computation, and quantum state synthesis*, Phys. Rev. Lett. **78**, 2252 (1997), [doi:10.1103/PhysRevLett.78.2252](https://doi.org/10.1103/PhysRevLett.78.2252), [arXiv:quant-ph/9611027](https://arxiv.org/abs/quant-ph/9611027).
  - [6] E. Knill, R. Laflamme, and W. H. Zurek, *Resilient quantum computation: Error models and thresholds*, Proc. Roy. Soc. London A **454**, 365 (1998), [arXiv:quant-ph/9702058](https://arxiv.org/abs/quant-ph/9702058), URL <http://www.jstor.org/stable/53171>.
  - [7] J. Preskill, *Fault-tolerant quantum computation*, in *Introduction to Quantum Computation and Information*, edited by H.-K. Lo, T. Spiller, and S. Popescu (World Scientific, Singapore / River Edge, NJ, 1998), chap. 8, pp. 213–269, ISBN 9-810-24410-X, [arXiv:quant-ph/9712048](https://arxiv.org/abs/quant-ph/9712048).
  - [8] J. Preskill, *Reliable quantum computers*, Proc. Roy. Soc. London A **454**, 385 (1998), [arXiv:quant-ph/9705031](https://arxiv.org/abs/quant-ph/9705031), URL <http://www.jstor.org/stable/53172>.
  - [9] A. M. Stephens, A. G. Fowler, and L. C. L. Hollenberg, *Universal fault tolerant quantum computation on bilinear nearest neighbor arrays*, Quant. Inf. Comp. **8**, 0330 (2008), [arXiv:quant-ph/0702201](https://arxiv.org/abs/quant-ph/0702201), URL <http://www.rintonpress.com/xxqic8/qic-8-34/0330-0344.pdf>.
  - [10] E. Knill, *Quantum computing with realistically noisy devices*, Nature **434**, 39 (2005), [doi:10.1038/nature03350](https://doi.org/10.1038/nature03350), [arXiv:quant-ph/0410199](https://arxiv.org/abs/quant-ph/0410199).
  - [11] E. Knill, *Fault-tolerant postselected quantum computa-*

- tion: Schemes (2004), [arXiv:quant-ph/0402171](#).
- [12] E. Knill, *Fault-tolerant postselected quantum computation: Threshold analysis* (2004), [arXiv:quant-ph/0404104](#).
  - [13] F. M. Spedalieri and V. P. Roychowdhury, *Latency in local, two-dimensional, fault-tolerant quantum computing*, *Quant. Inf. Comp.* **9**, 666 (2009), [arXiv:0805.4213](#), URL <http://www.rinton.net/xxqic9/qic-9-78/0666-0682.pdf>.
  - [14] D. Bacon, *Operator quantum error-correcting subsystems for self-correcting quantum memories*, *Phys. Rev. A* **73**, 012340 (2006), [doi:10.1103/PhysRevA.73.012340](#), [arXiv:quant-ph/0506023v4](#).
  - [15] A. Y. Kitaev, *Quantum error correction with imperfect gates*, in *Proceedings of the Third International Conference on Quantum Communication, Computing and Measurement*, edited by O. Hirota, A. S. Holevo, and C. M. Caves (Plenum Press, New York, 1997).
  - [16] E. Dennis, A. Kitaev, A. Landahl, and J. Preskill, *Topological quantum memory*, *J. Math. Phys.* **43**, 4452 (2002), [doi:10.1063/1.1499754](#), [arXiv:quant-ph/0110143](#).
  - [17] R. Raussendorf and J. Harrington, *Fault-tolerant quantum computation with high threshold in two dimensions*, *Phys. Rev. Lett.* **98**, 190504 (2007), [doi:10.1103/PhysRevLett.98.190504](#), [arXiv:quant-ph/0610082](#).
  - [18] A. G. Fowler, A. M. Stephens, and P. Groszkowski, *High-threshold universal quantum computation on the surface code*, *Phys. Rev. A* **80**, 052312 (2009), [doi:10.1103/PhysRevA.80.052312](#), [arXiv:0803.0272](#).
  - [19] D. S. Wang, A. G. Fowler, and L. C. L. Hollenberg, *Surface code quantum computing with error rates over 1%*, *Phys. Rev. A* **83**, 020302(R) (2011), [doi:10.1103/PhysRevA.83.020302](#), [arXiv:1009.3686](#).
  - [20] H. Bombin and M. A. Martin-Delgado, *Topological quantum distillation*, *Phys. Rev. Lett.* **97**, 180501 (2006), [doi:10.1103/PhysRevLett.97.180501](#), [arXiv:quant-ph/0605138](#).
  - [21] *List of uniform tilings*, URL [http://en.wikipedia.org/wiki/List\\_of\\_uniform\\_tilings](http://en.wikipedia.org/wiki/List_of_uniform_tilings).
  - [22] D. S. Wang, A. G. Fowler, C. D. Hill, and L. C. L. Hollenberg, *Graphical algorithms and threshold error rates for the 2d color code*, *Quant. Inf. Comp.* **10**, 780 (2010), [arXiv:0907.1708](#), URL <http://www.rintonpress.com/xxqic10/qic-10-910/0780-0802.pdf>.
  - [23] H. G. Katzgraber, H. Bombin, and M. A. Martin-Delgado, *Error threshold for color codes and random three-body ising models*, *Phys. Rev. Lett.* **103**, 090501 (2009), [doi:10.1103/PhysRevLett.103.090501](#), [arXiv:0902.4845](#).
  - [24] G. Duclos-Cianci, H. Bombin, and D. Poulin, *Fast decoding algorithm for subspace and subsystem color codes and local equivalence of topological phases* (2011), personal communication.
  - [25] M. Ohzeki, *Accuracy thresholds of topological color codes on the hexagonal and square-octagonal lattices*, *Phys. Rev. E* **80**, 011141 (2009), [doi:10.1103/PhysRevE.80.011141](#), [arXiv:0903.2102](#).
  - [26] R. S. Andrist, H. G. Katzgraber, H. Bombin, and M. A. Martin-Delgado, *Tricolored lattice gauge theory with randomness: Fault-tolerance in topological color codes* (2010), [arXiv:1005.0777](#).
  - [27] C. Wang, J. Harrington, and J. Preskill, *Confinement-Higgs transition in a disordered gauge theory and the accuracy threshold for quantum memory*, *Ann. Phys.* **303**, 31 (2003), [doi:10.1016/S0003-4916\(02\)00019-2](#), [arXiv:quant-ph/0207088](#).
  - [28] M. Ohzeki, *Locations of multicritical points for spin glasses on regular lattices*, *Phys. Rev. E* **79**, 021129 (2009), [doi:10.1103/PhysRevE.79.021129](#), [arXiv:0811.0464](#).
  - [29] T. Ohno, G. Arakawa, I. Ichinose, and T. Matsui, *Phase structure of the random-plaquette  $z_2$  gauge model: accuracy threshold for a toric quantum memory*, *Nucl. Phys. B* **697**, 462 (2004), [doi:10.1016/j.nuclphysb.2004.07.003](#), [arXiv:quant-ph/0401101](#).
  - [30] S. L. A. de Queiroz, *Location and properties of the multicritical point in the Gaussian and  $\pm j$  Ising spin glasses*, *Phys. Rev. B* **79**, 174408 (2009), [doi:10.1103/PhysRevB.79.174408](#), [arXiv:0902.4153](#).
  - [31] M. Suchara, S. Bravyi, and B. Terhal, *Constructions and noise threshold of topological subsystem codes* (2010), [arXiv:1012.0425](#).
  - [32] H. Bombin, *Topological subsystem codes*, *Phys. Rev. A* **81**, 032301 (2010), [doi:10.1103/PhysRevA.81.032301](#), [arXiv:0908.4246](#).
  - [33] E. Berlekamp, R. J. McEliece, and H. van Tilborg, *On the inherent intractability of certain coding problems*, *IEEE Trans. Info. Theo.* **24**, 384 (1978), [doi:10.1109/TIT.1978.1055873](#).
  - [34] J. E. Levy, A. Ganti, C. A. Phillips, B. R. Hamlet, A. J. Landahl, T. M. Gurrieri, R. D. Carr, and M. S. Carroll, *Brief announcement: the impact of classical electronics constraints on a solid-state logical qubit memory*, in *Proceedings of the Twenty-First Annual ACM Symposium on Parallelism in Algorithms and Architectures*, edited by F. Meyer auf der Heide and M. A. Bender (ACM Press, New York, 11–13 August, 2009, Calgary, AB, Canada, 2009), ISBN 978-1-60558-606-9, [doi:10.1145/1583991.1584039](#), [arXiv:0904.0003](#).
  - [35] J. E. Levy, M. S. Carroll, A. Ganti, C. A. Phillips, A. J. Landahl, T. M. Gurrieri, R. D. Carr, H. L. Stalford, and E. Nielsen, *Implications of electronics constraints for solid-state quantum error correction and quantum circuit failure probability* (2011), [arXiv:1105.0682](#).
  - [36] M. A. Nielsen and I. L. Chuang, *Quantum Computation and Quantum Information* (Cambridge University Press, Cambridge, 2000), ISBN 0-521-63235-8 (Hardback), 0-521-63503-9 (Paperback).
  - [37] J. Preskill, *Lecture notes for Caltech Ph 219: Quantum Information and Computation* (1998), URL <http://www.theory.caltech.edu/~preskill/ph219/>.
  - [38] P. Aliferis, D. Gottesman, and J. Preskill, *Quantum accuracy threshold for concatenated distance-3 codes*, *Quant. Inf. Comp.* **6**, 97 (2006), [arXiv:quant-ph/0504218](#), URL <http://www.rinton.net/xxqic6/qic-6-2/097-165.pdf>.
  - [39] P. Aliferis and A. W. Cross, *Subsystem fault tolerance with the Bacon-Shor code*, *Phys. Rev. Lett.* **98**, 220502 (2007), [doi:10.1103/PhysRevLett.98.220502](#), [arXiv:quant-ph/0610063](#).
  - [40] P. Aliferis, D. Gottesman, and J. Preskill, *Accuracy threshold for postselected quantum computation*, *Quant. Inf. Comp.* **8**, 0181 (2008), [arXiv:quant-ph/0703264](#), URL <http://www.rintonpress.com/xxqic8/qic-8-34/0181-0244.pdf>.
  - [41] P. Aliferis and J. Preskill, *Fibonacci scheme for fault-tolerant quantum computation*, *Phys. Rev. A*

- 79, 012332 (2009), [doi:10.1103/PhysRevA.79.012332](https://doi.org/10.1103/PhysRevA.79.012332), [arXiv:0809.5063](https://arxiv.org/abs/0809.5063).
- [42] A. W. Cross, D. P. DiVincenzo, and B. M. Terhal, *Comparative code study for quantum fault tolerance*, Quant. Inf. Comp. **9**, 541 (2009), [arXiv:0711.1556](https://arxiv.org/abs/0711.1556), URL <http://www.rinton.net/xxqic9/qic-9-78/0541-0572.pdf>.
- [43] P. Aliferis and J. Preskill, *Fault-tolerant quantum computation against biased noise*, Phys. Rev. A **78**, 052331 (2008), [doi:10.1103/PhysRevA.78.052331](https://doi.org/10.1103/PhysRevA.78.052331), [arXiv:0710.1301](https://arxiv.org/abs/0710.1301).
- [44] D. Gottesman, *The Heisenberg representation of quantum computers*, in *Group22: Proceedings of the XXII International Colloquium on Group Theoretical Methods in Physics*, edited by S. P. Corney, R. Delbourgo, and P. D. Jarvis (International Press, Cambridge, MA, 13–17 Jul. 1998, Hobart, Australia, 1999), pp. 32–43, [arXiv:quant-ph/9807006](https://arxiv.org/abs/quant-ph/9807006).
- [45] A. M. Steane, *Error correcting codes in quantum theory*, Phys. Rev. Lett. **77**, 793 (1996), [doi:10.1103/PhysRevLett.77.793](https://doi.org/10.1103/PhysRevLett.77.793).
- [46] A. M. Steane, *Space, time, parallelism and noise requirements for reliable quantum computing*, Fortsch. Phys. **46**, 443 (1998), [arXiv:quant-ph/9708021](https://arxiv.org/abs/quant-ph/9708021), URL <http://onlinelibrary.wiley.com/doi/10.1002/%28SICI%291521-3978%28199806%2946:4%3C443::AID-PROP443%3E3.0.CO;2-8/abstract>.
- [47] A. R. Calderbank and P. W. Shor, *Good quantum error-correcting codes exist*, Phys. Rev. A **54**, 1098 (1996), [doi:10.1103/PhysRevA.54.1098](https://doi.org/10.1103/PhysRevA.54.1098), [arXiv:quant-ph/9512032](https://arxiv.org/abs/quant-ph/9512032).
- [48] A. Steane, *Multiple particle interference and quantum error correction*, Proc. Roy. Soc. London A **452**, 2551 (1996), [arXiv:quant-ph/9601029](https://arxiv.org/abs/quant-ph/9601029), URL <http://www.jstor.org/stable/52827>.
- [49] A. G. Fowler, *Two-dimensional color-code quantum computation*, Phys. Rev. A **83**, 042310 (2011), [doi:10.1103/PhysRevA.83.042310](https://doi.org/10.1103/PhysRevA.83.042310), [arXiv:0806.4827v3](https://arxiv.org/abs/0806.4827v3).
- [50] D. Gottesman, *Stabilizer codes and quantum error correction*, Ph.D. thesis, Caltech (1997), [arXiv:quant-ph/9705052](https://arxiv.org/abs/quant-ph/9705052).
- [51] A. G. Fowler, D. S. Wang, and L. C. L. Hollenberg, *Surface code quantum error correction incorporating accurate error propagation*, Quant. Inf. Comp. **11**, 8 (2011), [arXiv:1004.0255](https://arxiv.org/abs/1004.0255).
- [52] J. Harrington, personal communication about the accuracy threshold analysis done in support of Ref. [17].
- [53] H. Nishimori, *Internal energy, specific-heat and correlation-function of the bond-random Ising-model*, Prog. Theor. Phys. **66**, 1169 (1981), [doi:10.1143/PTP.66.1169](https://doi.org/10.1143/PTP.66.1169).
- [54] H. Nishimori, *Geometry-induced phase transition in the  $\pm j$  Ising model*, J. Phys. Soc. Japan **55**, 3305 (1986), [doi:10.1143/JPSJ.55.3305](https://doi.org/10.1143/JPSJ.55.3305).
- [55] J. C. Pezzullo, *Nonlinear least squares regression (curve fitter)* (2011), (Online calculator), URL <http://statpages.org/nonlin.html>.
- [56] I. Jensen and A. J. G. and, *Self-avoiding walks, neighbour-avoiding walks and trails on semiregular lattices*, J. Phys. A: Math. Gen. **31**, 8137 (1998), [doi:10.1088/0305-4470/31/40/008](https://doi.org/10.1088/0305-4470/31/40/008).
- [57] I. Jensen, *Improved lower bounds on the connective constants for two-dimensional self-avoiding walks*, J. Phys. A: Math. Gen. **37**, 11521 (2004), [doi:10.1088/0305-4470/37/48/001](https://doi.org/10.1088/0305-4470/37/48/001).
- [58] S. E. Alm, *Upper and lower bounds for the connective constants of self-avoiding walks on the Archimedean and Laves lattices*, J. Phys. A: Math. Gen. **38**, 2055 (2005), [doi:10.1088/0305-4470/38/10/001](https://doi.org/10.1088/0305-4470/38/10/001).
- [59] B. Eastin, *Error channels and the threshold for fault-tolerant quantum computation*, Ph.D. thesis, University of New Mexico (2007), [arXiv:0710.2560](https://arxiv.org/abs/0710.2560).
- [60] E. Knill, R. Laflamme, and W. H. Zurek, *Threshold accuracy for quantum computation* (1996), [arXiv:quant-ph/9610011](https://arxiv.org/abs/quant-ph/9610011).
- [61] S. Bravyi and A. Kitaev, *Universal quantum computation with ideal Clifford gates and noisy ancillas*, Phys. Rev. A **71**, 022316 (2005), [doi:10.1103/PhysRevA.71.022316](https://doi.org/10.1103/PhysRevA.71.022316), [arXiv:quant-ph/0403025](https://arxiv.org/abs/quant-ph/0403025).
- [62] B. Eastin and E. Knill, *Restrictions on transversal encoded quantum gate sets*, Phys. Rev. Lett. **102**, 110502 (2009), [doi:10.1103/PhysRevLett.102.110502](https://doi.org/10.1103/PhysRevLett.102.110502), [arXiv:0811.4262](https://arxiv.org/abs/0811.4262).
- [63] H. Bombin and M. A. Martin-Delgado, *Topological computation without braiding*, Phys. Rev. Lett. **98**, 160502 (2007), [doi:10.1103/PhysRevLett.98.160502](https://doi.org/10.1103/PhysRevLett.98.160502), [arXiv:quant-ph/0610024](https://arxiv.org/abs/quant-ph/0610024).
- [64] B. W. Reichardt, *Quantum universality by state distillation* (2006), [arXiv:quant-ph/0608085](https://arxiv.org/abs/quant-ph/0608085).
- [65] H. Buhrman, R. Cleve, M. Laurent, N. Linden, A. Schrijver, and F. Unger, *New limits on fault-tolerant quantum computation*, in *Proceedings of the 47th IEEE Symposium on Foundations of Computer Science*, edited by B. Werner, IEEE (IEEE Press, Los Alamitos, CA, Oct. 21–24, Berkeley, CA, USA, 2006), pp. 411–419, ISBN 0-7695-2720-5, [doi:10.1109/FOCS.2006.50](https://doi.org/10.1109/FOCS.2006.50), [arXiv:quant-ph/0604141](https://arxiv.org/abs/quant-ph/0604141).
- [66] S. Virmani, S. F. Huelga, and M. B. Plenio, *Classical simulability, entanglement breaking, and quantum computation thresholds*, Phys. Rev. A **71**, 042328 (2005), [doi:10.1103/PhysRevA.71.042328](https://doi.org/10.1103/PhysRevA.71.042328), [arXiv:quant-ph/0408076](https://arxiv.org/abs/quant-ph/0408076).
- [67] R. Raussendorf, J. Harrington, and K. Goyal, *Topological fault-tolerance in cluster state quantum computation*, New J. Phys. **9**, 199 (2007), [doi:10.1088/1367-2630/9/6/199](https://doi.org/10.1088/1367-2630/9/6/199), [arXiv:quant-ph/0703143](https://arxiv.org/abs/quant-ph/0703143).
- [68] D. Poulin, *Stabilizer formalism for operator quantum error correction*, Phys. Rev. Lett. **95**, 230504 (2005), [doi:10.1103/PhysRevLett.95.230504](https://doi.org/10.1103/PhysRevLett.95.230504), [arXiv:quant-ph/0508131](https://arxiv.org/abs/quant-ph/0508131).
- [69] R. Raussendorf, J. Harrington, and K. Goyal, *A fault-tolerant one-way quantum computer*, Ann. Phys. **321**, 2242 (2006), [doi:10.1016/j.aop.2006.01.012](https://doi.org/10.1016/j.aop.2006.01.012), [arXiv:quant-ph/0510135](https://arxiv.org/abs/quant-ph/0510135).
- [70] G. Duclos-Cianci and D. Poulin, *Fast decoders for topological quantum codes*, Phys. Rev. Lett. **104**, 050504 (2010), [doi:10.1103/PhysRevLett.104.050504](https://doi.org/10.1103/PhysRevLett.104.050504), [arXiv:0911.0581](https://arxiv.org/abs/0911.0581).
- [71] J. Feldman, M. J. Wainwright, and D. R. Karger, *Using linear programming to decode binary linear codes*, IEE Trans. Info. Theo. **51**, 954 (2005), [doi:10.1109/TIT.2004.842696](https://doi.org/10.1109/TIT.2004.842696).
- [72] Similarly, the three-dimensional color codes [63] offer a way to generate an infinite code family from the fifteen-qubit Reed-Muller code by a means other than concatenation.